Gemini-LIGHTS: herbig Ae/Be and massive T Tauri protoplanetary disks imaged with gemini planet imager

Rich, E.A.; Monnier, J.D.; Aarnio, A.; Laws, A.S.E.; Setterholm, B.R.; Wilner, D.J.; ... ; Zhu, Z.

Citation

Rich, E. A., Monnier, J. D., Aarnio, A., Laws, A. S. E., Setterholm, B. R., Wilner, D. J., … Zhu, Z. (2022). Gemini-LIGHTS: herbig Ae/Be and massive T Tauri protoplanetary disks imaged with gemini planet imager. *The Astronomical Journal*, *164*(3). doi:10.3847/1538-3881/ac7be4

The Astronomical Journal, 164:109 (25pp), 2022 September https://doi.org/10.3847/1538-3881/ac7be4

Gemini-LIGHTS: Herbig Ae/Be and Massive T Tauri Protoplanetary Disks Imaged with Gemini Planet Imager

Evan A. Rich[1], John D. Monnier[1], Alicia Aarnio[2], Anna S. E. Laws[3], Benjamin R. Setterholm[1], David J. Wilner[4], Nuria Calvet[1], Tim Harries[3], Chris Miller[1], Claire L. Davies[3], Fred C. Adams[1,5], Sean M. Andrews[4], Jaehan Bae[6], Catherine Espaillat[7], Alexandra Z. Greenbaum[8], Sasha Hinkley[3], Stefan Kraus[3], Lee Hartmann[1], Andrea Isella[9], Melissa McClure[10], Rebecca Oppenheimer[11], Laura M. Pérez[12], and Zhaohuan Zhu[13]

[1] Department of Astronomy, University of Michigan, West Hall, 1085 South University Avenue, Ann Arbor, MI 48109-1090, USA; earich@umich.edu
[2] The University of North Carolina at Greensboro, USA
[3] Astrophysics Group, University of Exeter, Stocker Road, Exeter, EX4 4QL, UK
[4] Center for Astrophysics | Harvard & Smithsonian, 60 Garden Street, Cambridge, MA 02138, USA
[5] Physics Department, University of Michigan, Randall Lab, 450 Church Street, Ann Arbor, MI 48109-1090, USA
[6] Department of Astronomy, University of Florida, Gainesville, FL 32611, USA
[7] Department of Astronomy & Institute for Astrophysical Research, Boston University, 725 Commonwealth Avenue, Boston, MA 02215, USA
[8] IPAC, Caltech, 1200 E California Boulevard, Pasadena, CA 91125, USA
[9] Department of Physics and Astronomy, Rice University, 6100 Main Street, MS-108, Houston, TX 77005, USA
[10] Leiden Observatory, Leiden University, 2300 RA Leiden, The Netherlands
[11] Astrophysics Department, American Museum of Natural History, Central Park West at 79th Street, New York, NY 10024, USA
[12] Departamento de Astronomía, Universidad de Chile, Camino El Observatorio 1515, Las Condes, Santiago, Chile
[13] Department of Physics and Astronomy, University of Nevada, Las Vegas, 4505 S. Maryland Parkway, Box 454002, Las Vegas, NV 89154-4002, USA

Received 2022 April 8; revised 2022 May 26; accepted 2022 May 27; published 2022 August 23

Abstract

We present the complete sample of protoplanetary disks from the Gemini- Large Imaging with the Gemini Planet Imager Herbig/T Tauri Survey, which observed bright Herbig Ae/Be stars and T Tauri stars in near-infrared polarized light to search for signatures of disk evolution and ongoing planet formation. The 44 targets were chosen based on their near- and mid-infrared colors, with roughly equal numbers of transitional, pre-transitional, and full disks. Our approach explicitly did not favor well-known, "famous" disks or those observed by the Atacama Large Millimeter/submillimeter Array, resulting in a less-biased sample suitable to probe the major stages of disk evolution during planet formation. Our optimized data reduction allowed polarized flux as low as 0.002% of the stellar light to be detected, and we report polarized scattered light around 80% of our targets. We detected point-like companions for 47% of the targets, including three brown dwarfs (two confirmed, one new), and a new super-Jupiter-mass candidate around V1295 Aql. We searched for correlations between the polarized flux and system parameters, finding a few clear trends: the presence of a companion drastically reduces the polarized flux levels, far-IR excess correlates with polarized flux for nonbinary systems, and systems hosting disks with ring structures have stellar masses $<3\,M_\odot$. Our sample also included four hot, dusty "FS CMa" systems, and we detected large-scale (>100 au) scattered light around each, signs of extreme youth for these enigmatic systems. Science-ready images are publicly available through multiple distribution channels using a new FITS file standard that has been jointly developed with members of the Very Large Telescope Spectro-polarimetric High-contrast Exoplanet Research team.

Unified Astronomy Thesaurus concepts: Protoplanetary disks (1300); Direct imaging (387); Exoplanets (498); Herbig Ae/Be stars (723); Circumstellar dust (236)

Supporting material: data behind figure, figure set

1. Introduction

Orbiting reservoirs of gas and dust are often observed around young stars and referred to as "protoplanetary" disks. As the name suggests, it has long been thought (e.g., Kant 1755) that planets form within such disks, though definitive evidence had been lacking until quite recently (PDS 70b,c: Keppler et al. 2018; Haffert et al. 2019). While the location for planet formation is not in doubt, the critical physical mechanisms at play are still hotly debated for a predictive theory of planet formation that can robustly explain the wild diversity seen in exoplanet demographics.

Protoplanetary disks were initially classified based on the shapes of their spectral energy distributions (SEDs). "Full disks" show a continuous spectrum resulting from thermal emission from ∼1500 K to 10 s of K. "Transition disks" contrast in the SED shape of "full disks" and lack near-infrared emissions due to a large gap or cavity close to the star (Strom et al. 1989; Calvet et al. 2002; Espaillat et al. 2014), possibly indicating planet formation or merely disk dissipation. With the advent of high-angular-resolution imaging by the Atacama Large Millimeter/submillimeter Array (ALMA) and with extreme adaptive optics systems on 8m class telescopes, a more complex picture emerges. Recent surveys such as the Disk Substructures at High Angular Resolution Project (DSHARP) and Disks ARound T Tauri Stars with SPHERE (DARTT-S) have revealed a host of substructure including spiral arms, rings, gaps, and nonazimuth asymmetries (Andrews et al. 2018; Avenhaus et al. 2018; Garufi et al. 2018).

These features can be interpreted as signposts of forming planets; however exoplanets are not directly detected with the exception of PDS 70 b,c (Keppler et al. 2018).

Here, we bring the power of "polarized differential imaging (PDI)" to the study of planet formation. PDI reveals faint light scattered off the disk surfaces, cavity walls, and other dust structures in the circumstellar environment, revealing the three-dimensional distributions of small dust grains (Avenhaus et al. 2018; Rich et al. 2021). When coupled with ALMA imaging, which is sensitive to large dust grains settled into the disk midplane, PDI can monitor how dust grains grow and evolve with time and search for differences for systems with different stellar masses. Also, as PDI is dependent on illumination, the polarized flux will be influenced by shadowing of the inner disk onto the outer disk (Debes et al. 2017; Rich et al. 2019; Labdon et al. 2019; Muro-Arena et al. 2020) and the flaring angle of the outer protoplanetary disk.

In this work, we define the Gemini Large Imaging with the Gemini Planet Imager Herbig/T Tauri Survey (Gemini-LIGHTS) sample of 44 Herbig Ae/Be and T Tauri protostars imaged in near-infrared scattered light with the GPI (Section 2). Our new survey complements existing surveys (e.g., Strategic Explorations of Exoplanets and Disks with Subaru; Tamura 2009; DARTT-S, Avenhaus et al. 2018) by better populating the high-mass range (Herbig Ae/Be stars; >3 $M_\odot$). We describe the reduction techniques utilized in our sample (Section 3) then present our calibrated images along with a descriptive analysis (Section 4). Next we limit our sample to targets with stellar masses between 1.4 and 8 $M_\odot$ to search for trends between polarized flux and system characteristics (Section 5). Finally we discuss what trends we observe in the sample to help explain Herbig Ae/Be and T Tauri evolution (Section 6).

2. Gemini-LIGHTS Sample

The Gemini-LIGHTS sample was chosen to represent a broad range of T Tauri and Herbig Ae/Be stars with different protoplanetary disk structures including transition, pre-transition, and full disks. First, the sample consists of objects that were R <9 mag (GPI wave front sensor limit) and with decl. between +20° to −80° (lower airmass). Next, we identified these targets with significant infrared excess based on a color–color diagram of Wide-field Infrared Survey Explorer (WISE) and Two Micron All Sky Survey (2MASS) colors as shown in Figure 1. Additionally, we chose targets over a range of colors to achieve a mixture of transitional and full disks. Transitional disk targets host less near-infrared flux than far-infrared flux associated with a gap in the inner disk. This upper left portion of the diagram coincides with the location of the full disks shown in Figure 1. Full disk targets host equal near-infrared flux to far-infrared flux associated with no gaps in the disk. We note that a systems inclination can effect their broad SED categorization. Known equal-brightness binaries were not selected with a separation between $0\farcs05$ and $2\farcs0$ because they would inhibit the performance of the adaptive optics (AO) system. Compact binaries (e.g., HD 34700A) and unequal brightness binaries (e.g., FU Ori) were not selected against. Observations were taken in the *J* and *H* bands; however not every object has both bands observed. *H*-band observations were prioritized for dim R-band stars for better AO performance; otherwise *J*-band observations were prioritized.

We also added archival observations of targets to our sample that have previously been observed by GPI. First we include an early science GPI project (Monnier et al. 2017), which includes data from MWC 275, HD 144432, MWC 863, and HD 169142. We have also included data found on the Gemini archive including targets PDS 66, HD 100546, HD 101412, HD 100453, HD 142527, and AK Sco, in which some have previously been published (Rodigas et al. 2014; Wagner et al. 2015; Follette et al. 2017).

The Gemini-LIGHTS sample includes 44 targets, which are summarized in Table 1, along with their stellar properties in Table 2, and photometry used for the sample selection in Table 3. Stellar properties are primarily taken from Vioque et al. (2018) to create a uniform sample. A Hertzprung–Russell (HR) diagram and histograms of the systems' properties are shown in Figure 1 where we also label which targets have masses >8 $M_\odot$, Herbig Ae/Be stars (>7600 K), and T Tauri stars (<7600 K). Targets have distances between 40 and 5000 pc with the median distance of 350 pc, target age estimates span from 0.02 to 15 Myr and a median age of 2.3 Myr, and target stellar masses range from 0.3 to 20 $M_\odot$ with a median value of 2.5 $M_\odot$. The majority of our sample have masses consistent with Herbig Ae/Be stars. Also, all but FU Ori (∼0.3 $M_\odot$) have central star masses larger than 1 $M_\odot$.

We note a limitation in our sample. We plot the estimated age versus stellar mass in Figure 1 and find that the two properties are highly correlated. This is likely due to our sample having few intermediate-mass T Tauri stars. This effect was noted by Guzmán-Díaz et al. (2020) where their recent survey of Herbig Ae/Be stars was also missing young intermediate-mass stars (see Figure 8 by Guzmán-Díaz et al. 2020).

2.1. Observations

Observations of the targets were taken at the Gemini South Observatory using the GPI (Macintosh et al. 2014; Poyneer et al. 2014; Larkin et al. 2014) in the *J*- and *H*-band filters. Observations were in the polarimetry mode using coronagraphic spots of sizes 184.7 mas and 246.7 mas for the *J* and *H* bands, respectively, and a pixel scale of 14.14 mas. Observations of the targets HD 100453 and HD 142527 were the only observations taken without a coronagraphic mask. Each image of a target measures the orthogonal polarization state of the $2\farcs0 \times 2\farcs0$ field of view (FOV). Between each image of a target, the half-wave plate is rotated $22\fdg5$. This creates a polarization set of four images at four different wave plate positions (0°, $22\fdg5$, 45°, $67\fdg5$). A typical observational epoch of a target observed eight sets of four polarization images producing 32 images per epoch. Exposure of the image for each target was adjusted for the targets brightness such that the PSF of the star does not saturate the images. Observations of the targets occurred between 2014 April and 2019 May with the majority of observations occurring between 2017 and 2019, and a list of the observations can be found in Table 4. Calibration files such as lamps and dark images were taken by the Gemini observatory staff every 2–4 weeks and accessed through the Gemini archive.

3. Data Reduction

The data were primarily reduced using the IDL based Data Reduction Pipeline (DRP; Maire et al. 2010; Perrin et al. 2014) using version 1.5.0 (rev c0cad3f), written to reduce the GPI data. We also employed our own Python-based wrapper, which

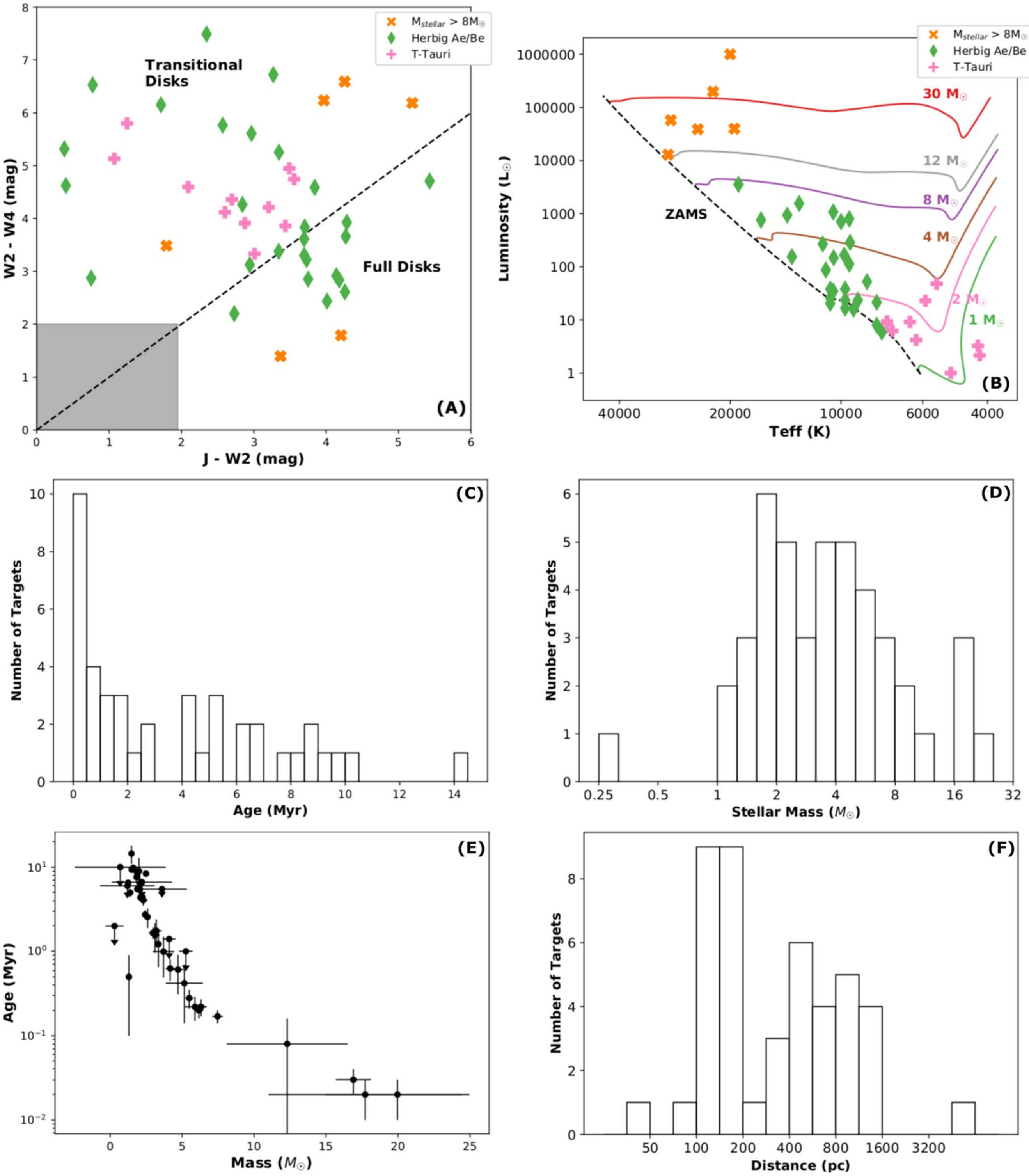

Figure 1. Sample parameters of the 44 targets in the Gemini-LIGHTS survey. (A) is an infrared color–color diagram using WISE and 2MASS colors. The dashed line represents a flat spectrum SED, and the gray shaded region are objects with no near-infrared or mid-infrared excess. (B) HR diagram with pre-main-sequence mass tracks (colored lines) and the zero-age main sequence (ZAMS) assuming solar-metallicity mass tracks from Bressan et al. (2012). Targets are classified as: stars with mass >8 M$_\odot$ (orange x's), T Tauri stars (pink plus), and Herbig Ae/Be stars (green diamonds). (C) Histogram of estimated age. (D) Histogram of estimated stellar mass. (E) Age vs. stellar mass. (F) Histogram of target distances. Specific target parameter values can be found in Appendix A in Tables 2 and 3. Note that FU Ori is not plotted on the HR diagram as the T_{eff} temperature is unknown.

automated the execution of the DRP IDL pipeline to batch process our data to allow for consistent and reproducible reductions. The Python wrapper edits the DRP parameter files needed and executes the IDL commands. Changes to the standard reduction were based on previous work by Monnier et al. (2019) and Laws et al. (2020). The Python wrapper is available on Github.[14]

---

[14] https://github.com/earich/Gemini_LIGHTS_pipeline

In order to reduce our raw observational data, we inspected the individual raw frames and removed any frames if there was poor Adaptive Optics (AO) performance or if the target star slips to the edge of the coronographic mask. If a single frame was removed or missing from a polarization set, a frame from an adjacent set was used in its place. If more than one frame from a polarization set was removed or missing, the entire polarization set is not used. From raw images to polarization data cubes (PODC) files, we utilized the IDL DRP without modifications as described by Maire et al. (2010), Perrin et al. (2014, 2015), Millar-Blanchaer et al. (2016), and De Rosa et al. (2020). Each PODC file contains two images of the orthogonal polarization states. After PODC files were created, each observation was inspected by eye to verify if the flexure solution was correct.

The PODC cubes are centered using the IDL DRP code, which utilizes a Radon transformation of the satellite spots to calculate the location of the star behind the coronagraph. We found that this transformation could fail when there was a bright point source in the field near the satellite spots. We found that applying a circular mask of radius = 10 pixels over the point source was sufficient to correct for this issue. We tested the centering function on point sources in the FOV around HD 50138 and found a centroid accuracy of 0.22 pix (3.1 mas). This method was applied to all targets with a point source in the FOV. All centering solutions were inspected by eye to ensure the method worked properly. There were two instances where the Radon transformation within IDL that DRP failed to find the correct center with the companion masking improvements. The coronographic mask for HD 98800 was placed over the A component of the system rather than the disk hosting B component of the system (Kennedy et al. 2019). We centered the images on the disk hosting B component using an interactive Radon transformation algorithm described by Monnier et al. (2017). Second, the centering uncertainty for MWC 863 was large (1.9 pixels) using the IDL DRP Radon transformation. Using the interactive Radon transformation used from Monnier et al. (2017) improved the centering measured by the companions center (>1.2 pixels). We found the best solution was taking the average centering position from the IDL DRP Radon transformation and correcting for relative offsets of the PODC frames by measuring the center of the companion resulting in a centroid accuracy of (0.4 pixels). The relative centering method with the companion comes at the cost of greater uncertainty for the absolute position of the star behind the coronographic mask.

We next create Stokes cubes (I,Q,U,V) from the derotated (north-up) PODC files. Each set of half-wave plate positions (four PODC files) are double differenced into Stokes I, Q, and U, creating a set of approximately eight Stokes cubes per observing epoch. We note that while a circular polarization (V) image is created in the DRP pipeline, we do not use it in our analysis and will not refer to V further in this work.

We removed stellar and instrumental polarization (SIP) from the Q and U images. Measuring the amount of SIP is typically done by picking a region in the image and measuring the ratio of Q_{SIP}/I and U_{SIP}/I, which we will refer to as f_Q and f_U, respectively. The shape of the SIP should be similar to the I image, when dominated by the PSF; thus we can remove the SIP by multiplying the fraction of f_Q and f_U polarization to the intensity image and subtracting it from the Q and U images creating a set of corrected Q^* and U^*

$$Q^* = Q - I \times f_Q, \tag{1}$$

$$U^* = U - I \times f_U, \tag{2}$$

where images have been corrected for SIP.

Next we picked a region in the image to best measure the SIP for each Q and U frame. As noted by Laws et al. (2020), using the region inside the coronagraphic mask region to estimate f_Q and f_U does not reliably remove the SIP for all targets. Laws et al. (2020) choose to use the region between 70 and 80 pixels away from the central star. This method is effective as long as the disk does not extend into this region or if there is a bright point source in this region. We chose to use a new method in which the entire FOV (0-140 pix) was used and mask out any regions where the Q/I or U/I ratio is larger than 0.05 or where there is known to be a point source within 10 pixels.

We tested if the masked method effectively measured f_Q and f_U by rotating the set of Stokes Q and U cubes into Q_ϕ and U_ϕ frames where:

$$Q_\phi = -Q^* \cos(2\phi) - U^* \sin(2\phi), \tag{3}$$

$$U_\phi = +Q^* \sin(2\phi) - U^* \cos(2\phi), \tag{4}$$

as defined by Monnier et al. (2019). This rotation will result in a distinctive quadrupole structure in Q_ϕ and U_ϕ. If the masked method left a quadrupole structure, we utilized annulus regions of 10 pixels wide that minimized the quadrupole structure in the Q_ϕ and U_ϕ images and recalculated Q^* and U^* described in Equations (1) and (2). These methods are compared in the appendix of Davies et al. (2022). Systems hosting bright point sources in the FOV occasionally exhibited some quadrupole structure in the Q_ϕ and U_ϕ that could not be removed with the above methods (e.g., HD 98800 B and HD 144432). Future work is needed to better remove SIP from the GPI polarimetric data. For those wishing to replicate our reductions, the regions used to calculate f_Q and f_U can be found in the headers of our reduced FITS images along with the average f_Q and f_U removed. The averages for a given epoch f_Q and f_U are listed in Table 4 as the polarization angle (PA) and % polarization. We note that this information can be used to investigate the unresolved polarization of the inner disk region but caution that targets with low % polarization (<0.6%) will be dominated by instrumental polarization (Millar-Blanchaer et al. 2016).

Once the SIP is finally removed, the final Q_ϕ and U_ϕ images are calculated, and the set of Q_ϕ and U_ϕ are median combined to produce the final I, Q_ϕ, and U_ϕ images as shown in Section 4. All I, Q_ϕ, and U_ϕ images for every epoch can be found as a figure set appearing on the online version of this work (Figure 2). An example of the I, Q_ϕ, and U_ϕ images can be seen in Figure 2. The fully reduced data can be found on Vizier and Data Behind the Figures (DBF). We also note that we have adopted a FITS header standard, in collaboration with the Very Large Telescope Spectro-polarimetric High-contrast Exoplanet Research (SPHERE) team members, which is presented in Appendix B to aid in easy comparison of data and result replication.

3.1. Flux Calibration

The images are flux calibrated using the four satellite spots in each of the PODC images. To increase the signal to noise of satellite spots, the PODC files are mean combined. For *H*-band

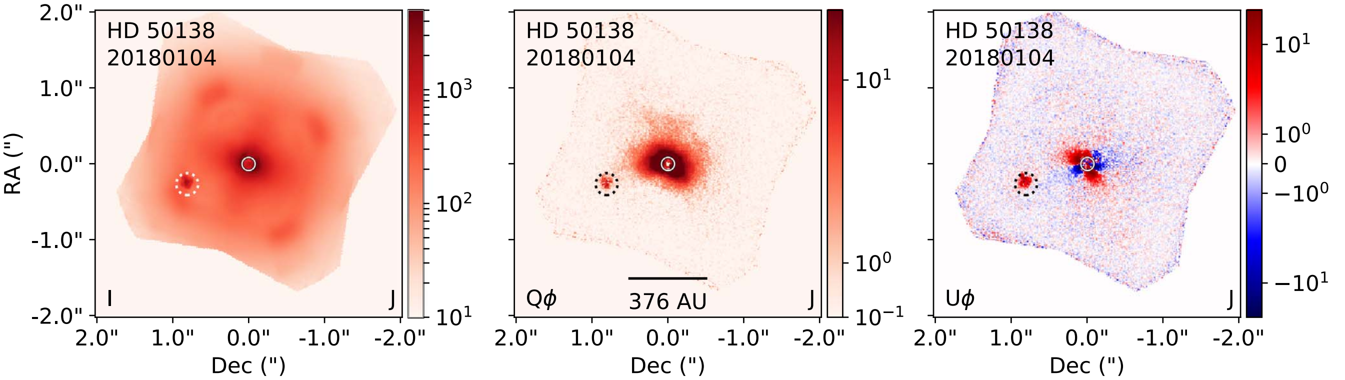

Figure 2. I, Q_ϕ , and U_ϕ images for the Gemini-LIGHTS sample. Coronagraphic mask region marked with black circle. Location of likely binaries indicated in dashed black circles. Target and epoch date (YYYYMMDD) indicated in the upper left of each panel. The complete figure set (44 figures) is available in the online journal.

(The data used to create this figure are available.)

(The complete figure set (44 images) is available.)

images, we used the first-order satellite spots. For *J*-band images, we used the second-order spots to ensure the spots were further away from the central PSF core. We note that the conversion factor between the satellite spots was updated since version 1.4 of DRP that was utilized by Laws et al. (2020) and Monnier et al. (2019). We used the known flux of the star from the 2MASS catalog to calculate the flux conversion factor and apply it to the Q_ϕ and U_ϕ images, as shown in Figure 3. In our sample, we measure an average scale factor of 3.05 ± 0.57 for the *J* band and 3.09 ± 0.51 for the *H* band $\mathrm{mJy}\,''^{-2}/(\mathrm{ADU/s})$. We note that time (s) in the above scale factor is the total exposure time (ITIME×coadds).

Central stars flux can be variable with time; thus without contemporaneous photometry we have taken effort to investigate and correct target epochs with discrepant flux calibration values. These different scale values could also be due to seeing conditions and AO performance. We investigated 14 observations that had a scale value 1σ (0.57 for the *J* band, 0.51 for the *H* band) away from the average scale value of 3.05 in the *J* band (3.09 in the *H* band). Four of these epochs had similar values to observations taken on the same night suggesting that the flux scale deviation is a correction for poor seeing or AO performance. Another four of these epochs had similar scale values to previous epochs suggesting that the divergent high or low scale value might be due to an over or underestimate of the flux of the target. The other six targets: FU Ori, HD 104237, HD 142666, HD 45677, HD 144432, and PDS 66 are likely to be due to variability; thus we use the average flux scale of other targets in that epoch. Finally, HD 100453 and HD 142527 were observed without coronographic spots; thus we choose to use flux calibration scale factors from Long et al. (2017) 0.836 $\mathrm{mJy}\,''^{-2}/(\mathrm{ADU/s})$ for both observations.

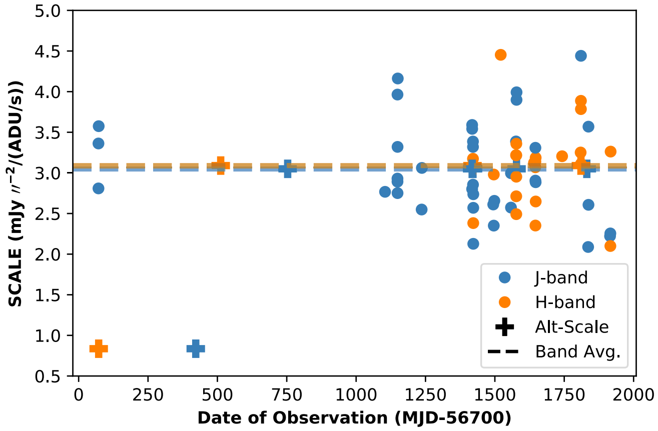

Figure 3. This figure shows the flux calibration scale for each of the targets and epochs in the sample. Blue dots are *J*-band observations, and orange dots are *H*-band observations. Observations that have their scale factors corrected (see Section 3.1) are noted with plus signs with their corrected values. Average *J*- and *H*-band scale factors are shown as dashed lines.

3.2. Flat-field Accuracy

Due to the design of the GPI instrument, flat-field corrections of the pixel-to-pixel variations in the raw frame are not currently possible. The current correction uses lamp flat observations to correct for low-frequency variations across the FOV. This issue was first investigated by Millar-Blanchaer et al. (2016). We observed the twilight sky to obtain sky flats in order to independently estimate the effects of the flat-field correction onto our data. We reduced the data using the same parameters as described above in Section 3. We plot an example of an individual Q and U frames as a % flux deviation from the average of the Q and U frames, as shown in Figure 4. We show that the low-frequency flat-field fails to correct for all large-scale flat-fielding variations, especially toward the edge of the detector. However, there are still sizable flux variations between 2%–4% at the center of the image. Thus we conclude that any azimuthal flux variations observed in the disk that are on the scale of 2%–4% may not be astrophysical but instrumental due to poor flat-fielding of the image.

3.3. Uncertainty Propagation

We estimate the uncertainty of our images by bootstrapping images from the fully reduced Stokes Q_ϕ and U_ϕ images. We performed this bootstrapping 100 times and these sets of bootstrapped images are used for all analysis and error propagation in Section 4 and utilized in calculating the uncertainties of the polarization statistics for each observed epoch as shown in Table 5.

3.4. Point-source Reduction

We identified point sources in the FOV by looking for bright companions in the intensity image and identifying dimmer

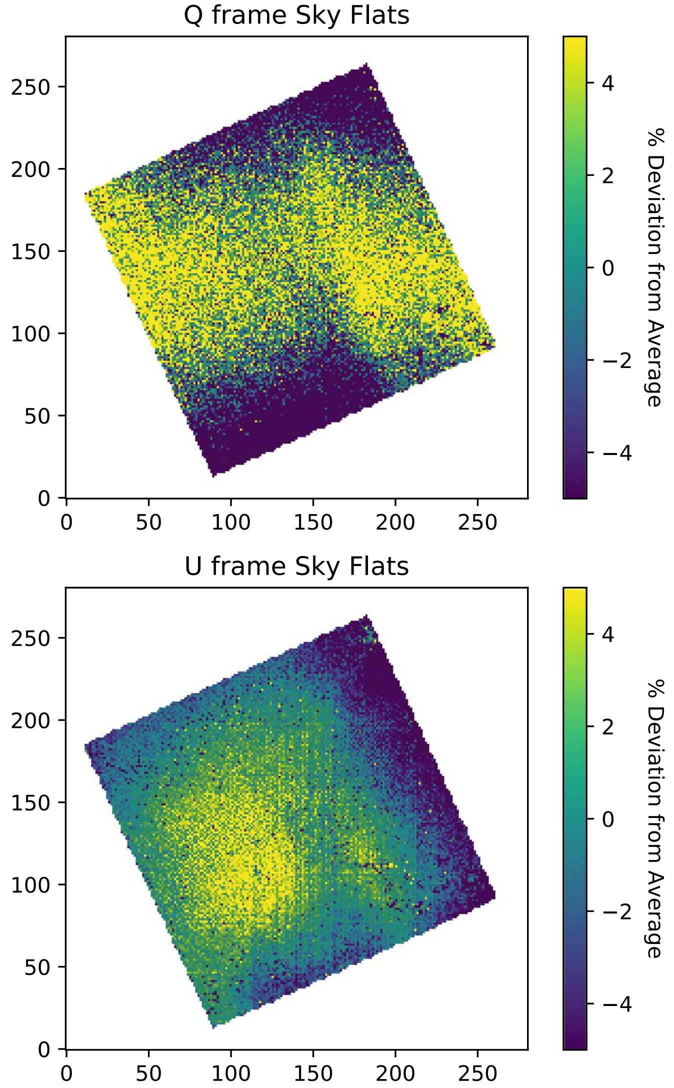

Figure 4. Showing the Q (top) and U (bottom) example sky flats taken on 2018 January 3. Flux plotted as the percent deviation from the flux average of the frame.

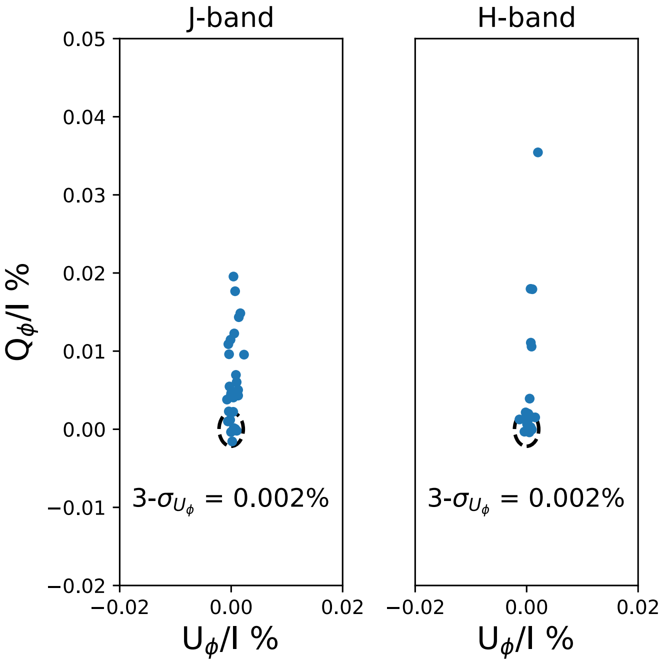

Figure 5. The % of Q_ϕ/I flux vs. U_ϕ/I in a $0\farcs4$ annulus (30 pixels) for *J*-band (left) and *H*-band (right) observations. The dashed circle represents the 3σ significance.

point sources using an angular differential imaging (ADI) reduction technique. For the ADI reduction, we used the Karhunen–Loéve image projection (KLIP) algorithm for epochs that had FOV rotation that was sufficiently large to take advantage of an ADI reduction. Using the centered PODC files from the standard reduction discussed above, we utilized the pyKLIP[15] package output (Wang et al. 2015). In order to avoid self-subtraction issues, we used parameters of subsection = 1 and annuli = 1, which minimize the number of individual segments in the FOV used to calculate the PSF. We found that 16 systems have point sources identified by the pyKLIP reduction. Upon close examination, all of these point sources are visible in the intensity images. A further 6 targets have point sources that were identified in the total intensity image but did not have sufficient FOV rotation for the pyKLIP analysis.

We measured the flux and position of each point source by fitting a Gaussian to each point source in the intensity frame. The location of these point sources can be found in Q_ϕ and U_ϕ images in the online figure sets (e.g., Figure 2) and are marked by dotted black circles. The point-source location, flux, and estimated mass are shown in Table 6. For the companion mass estimates we used models from Baraffe et al. (2015) for masses $>0.01\ M_\odot$ and the chemical equilibrium models from Phillips et al. (2020) for masses $<0.01\ M_\odot$.

Using the pyKLIP routine, we also placed limits on the point-source companions we are sensitive to detecting in our sample. We calculated the 5σ flux limit of point sources at angular separations of $0\farcs2$ and $0\farcs5$ for all targets with sufficient field rotation. We define sufficient rotation where a point source would move >1 pixel due to field rotation, corresponding to a total field rotation of 4° at $0\farcs2$ and 1.6° at $0\farcs5$. We note that 6 systems, HD 98800 B, HD 100453, HD 142527, HD 142666, HD 158643, and WRAY 15-535, did not have sufficient field rotation at $0\farcs2$ to determine the contrast at a separation of $0\farcs2$. Based on the contrast and the systems age, we estimated the upper limit mass that would be detectable at $0\farcs2$ and $0\farcs5$. For angular separations of $0\farcs2$, in 9 systems we can detect down to Jupiter-mass companions, for 26 we can detect down to brown dwarf mass companions, and in 3 systems we can detect some stellar mass companions. For angular separations of $0\farcs5$, in all systems we can detect companions down to 1 M_{jup} mass companions. The results for each epoch can be found in the appendix in Table 5. For the companion mass estimate limits we used models from Baraffe et al. (2015) for masses $>0.01\ M_\odot$ and the chemical equilibrium models from Phillips et al. (2020) for masses $<0.01\ M_\odot$.

4. Results

We now present the complete sample of our results from the Gemini-LIGHTS survey. All I, Q_ϕ , and U_ϕ images for all 71 epochs of the 44 targets can be found as a figure set appearing on the online version of this work (Figure 2). We will first identify targets in which we do not detect Q_ϕ flux. Next we will group the remaining targets by their disk morphological

---

[15] https://pyklip.readthedocs.io/en/latest/index.html

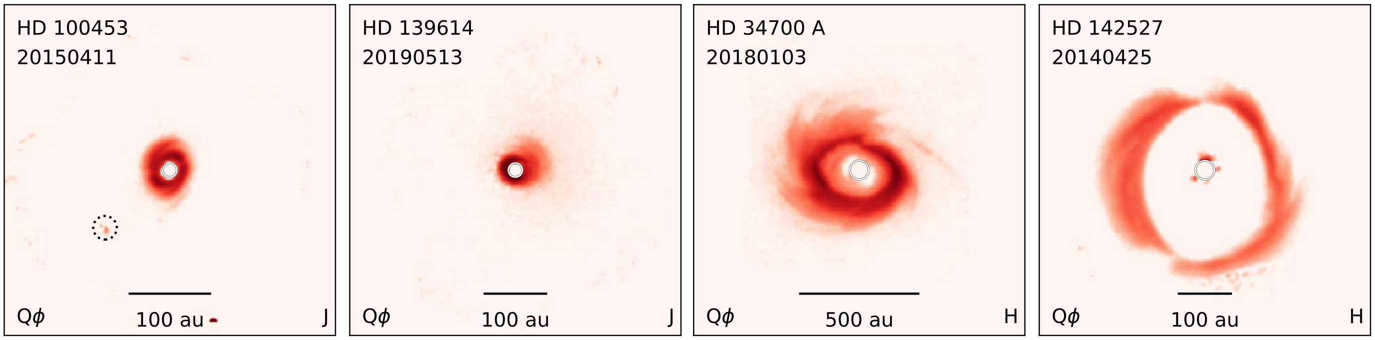

Figure 6. Spiraled Disks: Q_ϕ images of disks classified as hosting spiral arms including targets HD 100453, HD 139614, HD 34700 A, and HD 142527. See online figure sets (e.g., Figure 2 for target specific color bars). The image flux scale is log and chosen to highlight the target structure. The point sources in the FOV are labeled with a dashed black circle. The name of the target and the epoch in YYYYMMDD format can be found in the upper left of each image. The type of polarized image (Q_ϕ), the scale of the image (in au), and the photometry band (*J* or *H*) can be found along the bottom of each subimage.

properties. We note that some targets can be found in multiple categories.

Some of the observations from this long and large observational campaign have already been published as part of the Gemini-LIGHTS campaign. Laws et al. (2020) published observations of 4 large disks with irregular features (FU Ori, MWC 789, HD 45677, Hen 3-365). Monnier et al. (2019) investigated the *J*- and *H*-band observations of HD 34700A, which exhibit strong spiral structures. Davies et al. (2022) published the *J*- and *H*-band observations of HD 145718 that compared the scattered light images to photometry and near-IR interferometry and were constrained by radiative transfer modeling. Finally, Kraus et al. (2020) investigated the triple star system of GW Ori finding evidence of disk tearing.

4.1. Nondetections

Here we establish which targets have detected scattered light and which targets are nondetections. One advantage in rotating the polarization I, Q, and U into Q_ϕ and U_ϕ is the ease of interpretation. The Q_ϕ flux should be dominated by photons that scattered only once and from one source, while the U_ϕ flux could be dominated by photons that scattered multiple times, or scattering that is not azimuthally symmetric with the assumed central star (i.e., presence of a binary). We compute the amount of Q_ϕ and U_ϕ flux within $0\overset{\prime\prime}{.}4$ (30 pixels) divided by the stellar flux for that given band. For sources with no close-in point source (e.g., within $0\overset{\prime\prime}{.}4$ of central star), for disks with very low Q_ϕ, the amount of U_ϕ will go to zero before Q_ϕ, as shown in Figure 5. As Q_ϕ and U_ϕ are drawn from the same observables, the noise in Q_ϕ is the same as U_ϕ. Thus we look at the standard deviation of U_ϕ for epochs $<0.01\%$ Q_ϕ and U_ϕ and removed binaries by removing epochs $>3\sigma$. We then took the standard deviation of the summed U_ϕ flux, which is also the uncertainty of the Q_ϕ flux. Using this metric, we establish that we do not detect polarized light around 18 of the 77 epochs using a 3σ deviation of U_ϕ of 0.002% in the *J* band and 0.002% in the *H* band. Targets that are nondetections include: HD 36917, HD 101412, HD 144432, HD 158643, HD 176386, Hen 2-225, Hen 3-1330, MWC 147, MWC 166. Two targets, V1295 Aql (20180608 *H* band, 20180816 *H* band) and TY CrA (20180608 *H* band) where not detected in some epochs but were detected in other epochs (V1295 Aql: 20180816 *J* band; TY CrA: 20180817 *H* band). Thus, we do not detect polarization light around 9 of the 44 targets and additionally do not always detect polarization light in 2 of the targets.

4.2. Disk Structure Categorization

We are categorizing our disks only by the observed disk structure in the Q_ϕ images. The categories include spiral armed disks, ringed disks, continuous disks, irregular disks, and undetermined disks structure. Our chosen categories are inspired by the disk structure categories defined by Garufi et al. (2018). We have deviated when appropriate to better describe our sample. The results of our classification are tabulate in the appendix in Table 2.

4.2.1. Spiral Armed Disks

We find there are four targets that host one or more spiral arms including HD 100453, HD 139614, HD 34700 A, and HD 142527, as shown in Figure 6. HD 100453 hosts symmetric spiral arms, while HD 34700A and HD 142527 most multiple arms that are not symmetric. HD 139614 has an arm structure on one side of the disk. All four of these systems have had the origin of their spiral arms investigated previously (HD 100453: Wagner et al. 2015; HD 139614: Laws et al. 2020; HD 34700 A: Monnier et al. 2019; A. S. E. Laws 2022, in preparation; HD 142527: Long et al. 2017).

4.2.2. Ringed Disks

We define disks that have one or more concentric polarized light dust rings in their Q_ϕ image, as shown in Figure 7. We note that we deviate from the definition of Garufi et al. (2018) as they make a distinction between ringed and rimmed systems; however scattered light imaging lacks the information to robustly make the distinction due to the inner working angle. We find that seven targets show signatures of rings: HD 169142, HD 141569, MWC 275, CU Cha, HD 34700 A, HD 142527, and PDS 66. We note that two of the four spiral armed disks are also ringed disks (HD 142527, HD 34700 A).

4.2.3. Continuous Disks

We define continuous disks as disks that are resolved and do not appear to have a gap or hole in their PDI or show a strong nonazimuthal structure, as shown in Figure 8. Some of these disks may have a gap or ringed structure, but it is not shown in the polarized light imagery due to the inclination (HD 145718: Davies et al. 2022) or inner working angle (IWA; MWC 614: Kluska et al. 2018). We note that this does not imply that these disks do not have gaps at all, but those gaps are not visible in our polarized light imaging. We find that 11 targets show

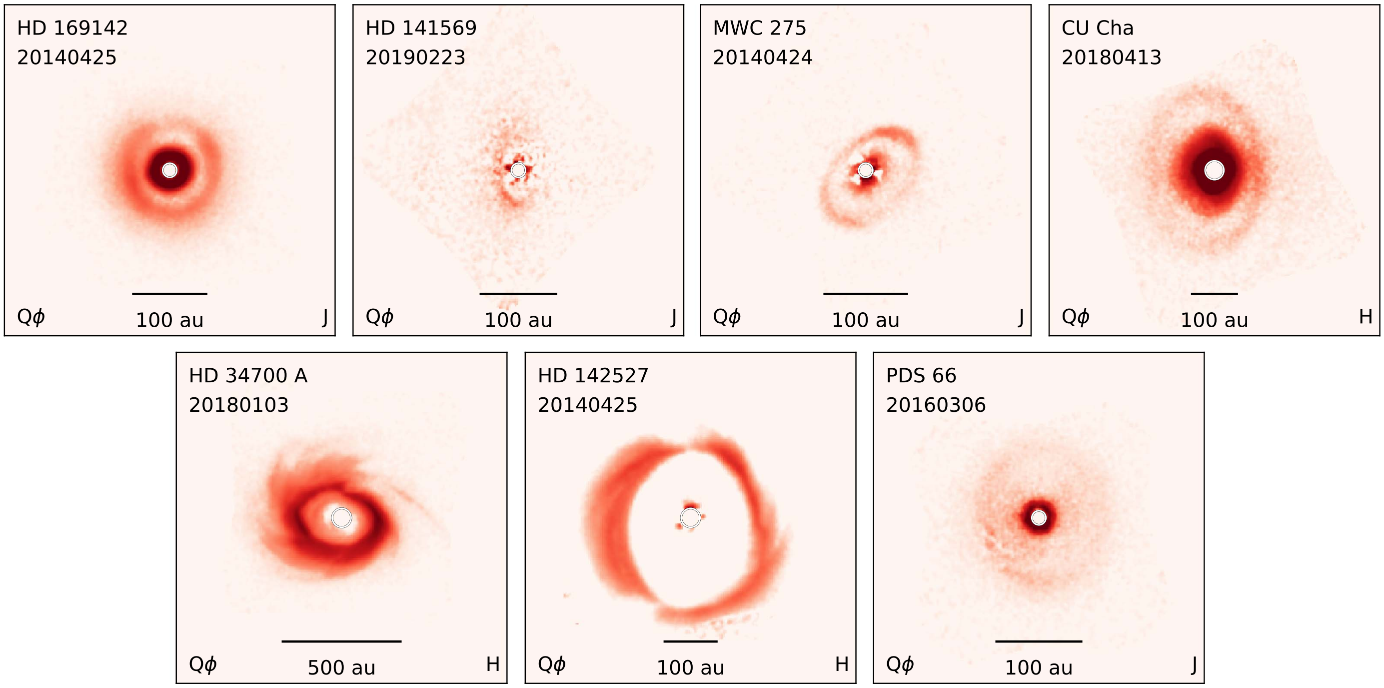

Figure 7. Ringed Disks: Q_ϕ images of disks classified as hosting rings including targets HD 169142, HD 141569, MWC 275, CU Cha, HD 34700 A, HD 142527, PDS 66. See online figure sets (e.g., Figure 2 for target specific color bars). See Figure 6 caption for figure details.

signatures of rings: AK Sco, HD 45677, HD 50138, HD 100453, HD 100546, HD 139614, HD 142666, HD 145718, HT Lup, MWC 297, and MWC 614. We note that one of the spiral armed disks are also continuous disks (HD 139614).

4.2.4. Irregulars

We define irregular disks as disks that host structures that have strong nonazimuthal features and disks that are very large in size (>300 au). There are four disks in our sample that exhibit these features: MWC 789, FU Ori, GW Ori, and Hen 3-365, which are shown in Figure 9. GW Ori irregularity is thought to be due to disk tearing as investigated by Kraus et al. (2020).

4.2.5. Undetermined

There are some targets that have a significant amount of polarized light detected (see Section 4.1); however the polarized light in the image does not extend far enough away to reliably categorize the disk into one of the above categories. Objects that fit this description include: HD 37806, HD38087, HD 85567, HD 95881, HD 98922, HD98800, HD 104237, HR 5999, MWC 863, TY CrA, V921 Sco, V1295 Aql, and WRAY 15-535, as shown in Figure 10. We note this is a similar to the "small disk" category utilized by Garufi et al. (2018). However, our sample is not strictly distance limited; thus some objects have disks that do appear to be small (e.g., HD 104237 disk radius <21 au), while other objects such as V921 Sco appear to be distant and have rather large disks (<300 au). Thus we choose to classify these objects as undetermined.

4.2.6. Categorization Summary

Utilizing the polarized disk morphology described above, we now investigate if we see any trends with the disk morphology. We plotted all 44 targets on an HR diagram and an infrared color–color diagram in Figure 11. We note that targets can be in multiple categories. The first trend is that ringed systems only occur in systems with masses $<3\ M_\odot$. This could partially be due to a distance effect where the ringed structure is within the IWA of the observations, though less likely as there are six systems with resolved disks that do not exhibit any ringed structures. Second, irregular systems appear to be younger; however, this is not a definitive trend as only three objects on the HR diagram are classified as irregular.

Next, we plot the complete sample on a color–color diagram as shown in Figure 11. We generally find that full disks are unresolved, undetected, or continuous disks. Pre-transitional disks are mostly continuous disks with some irregulars and ring disks. Finally, transitional disks are dominated by ringed disks, as expected.

4.3. FS CMa stars

Four of our targets have been identified as FS CMa targets, which are a subtype of B[e] stars: HD 45677, HD 50138, HD 85567, and HD 98922 (Miroshnichenko et al. 2007; Vioque et al. 2020). These stars are potentially post-main-sequence stars. We note that HD 45677 is also known as FS CMa, the prototype for this classification. We have the first resolved images of the dust around HD 45677, HD 50138, HD 85567, and HD 98922, as shown in Figure 12. All objects have significant Q_ϕ flux that is detected out to sizable distances of ∼250 au (HD 50138), ∼700 au (HD 45677), ∼300 au (HD 85567), and ∼180 au (HD 98922). Additionally, each of the objects also show significant U_ϕ flux, which is suggestive of multiple scatterings due to optical depth effects or multiple illumination sources due to a binary. The U_ϕ flux for both HD 45677 and HD 50138 is likely to be due to optical depth effects as the pattern is within the location of high Q_ϕ flux similarly seen in other optically thick sources such as HD 34700 A, GW Ori, and HD 100546. HD 50138 does have a point source

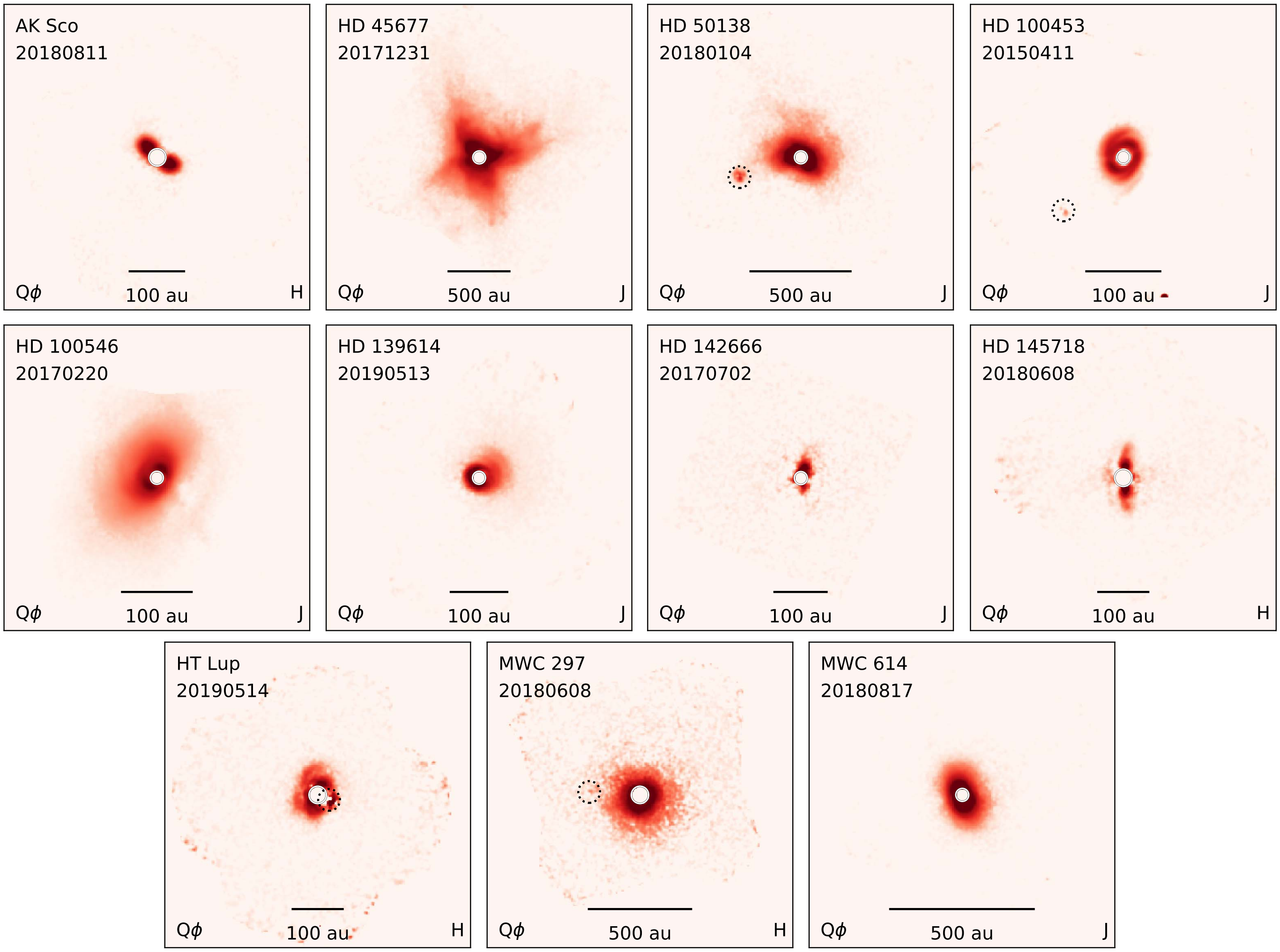

Figure 8. Continuous Disks: Q_ϕ images of disks classified as continuous including targets: AK Sco, HD 45677, HD 50138, HD 100453, HD 100546, HD 139614, HD 142666, HD 145718, HT Lup, MWC 297, and MWC 614. See online figure sets (e.g., Figure 2 for target specific color bars). See Figure 6 caption for figure details.

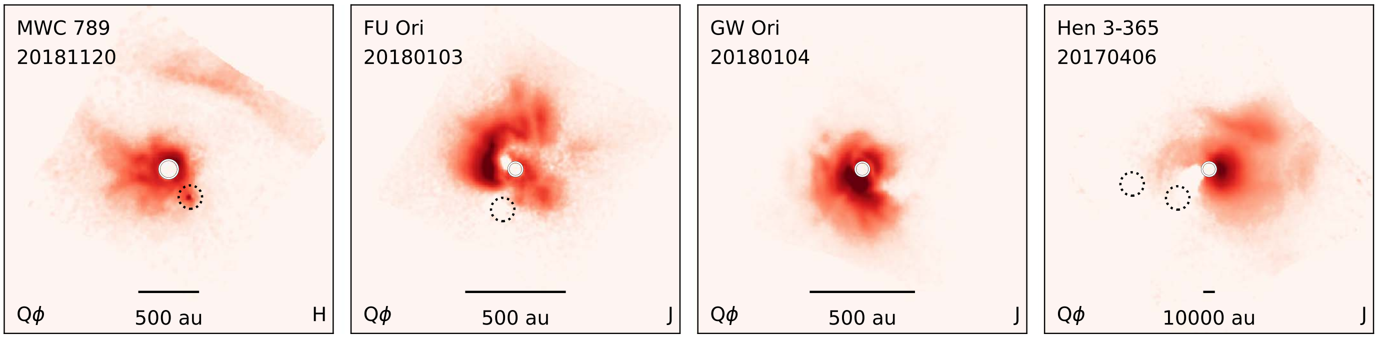

Figure 9. Irregular Disks: Q_ϕ images of disks classified including targets: MWC 789, FU Ori, GW Ori, and Hen 3-365. See online figure sets (e.g., Figure 2 for target specific color bars). See Figure 6 caption for figure details.

located within 1.″0 of the central star but is not co-located with the concentric Q_ϕ flux around the central star. There is excess polarized flux north of the main disk that could be faint additional structure (e.g., back of the disk, spiral arm), but we are unable to definitively determine its origin. HD 85567 is very distant (1047 pc); thus only the very outer portion of the system is imaged. Finally, HD 98922 exhibits a centrosymmetric Q_ϕ pattern around the inner working angle.

4.4. Point-source Detections in the Field of View

We found 24 point sources within the FOV of the PDI images with 21 targets hosting these point sources. Point sources are identified in Q_ϕ and U_ϕ images in the online figure sets (e.g., Figure 2) with a dotted black circle marking the companions locations. The values are also tabulated in Table 6 located in the appendix. We assessed the likelihood that a given point source was a background star from the measured separation and

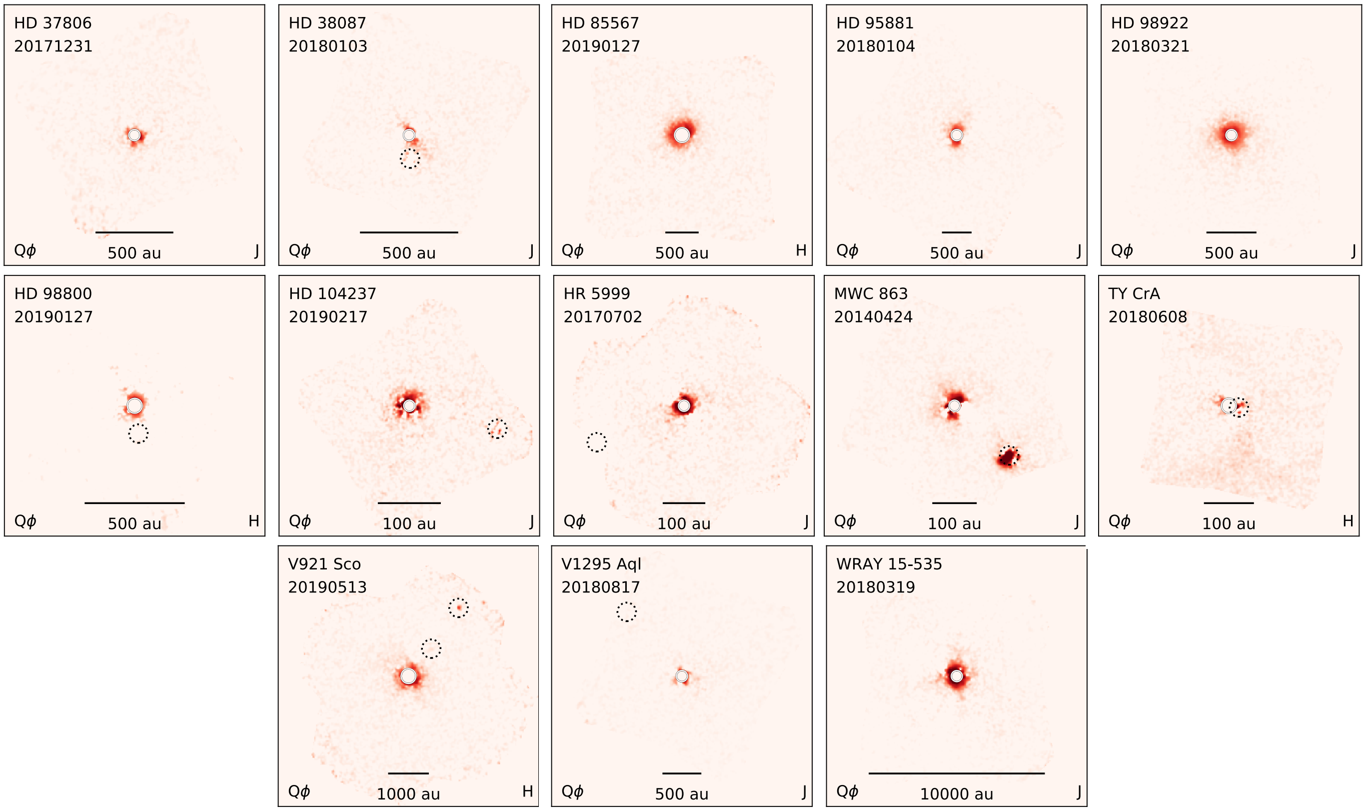

Figure 10. Undetermined disk structures: Q_ϕ images of disks that are insufficiently resolved to determine their morphology. Targets include: HD 37806, HD38087, HD 85567, HD 95881, HD 98922, HD98800, HD 104237, HR 5999, MWC 863, TY CrA, V921 Sco, V1295 Aql, and WRAY 15-535. See online figure sets (e.g., Figure 2 for target specific color bars). See Figure 6 caption for figure details.

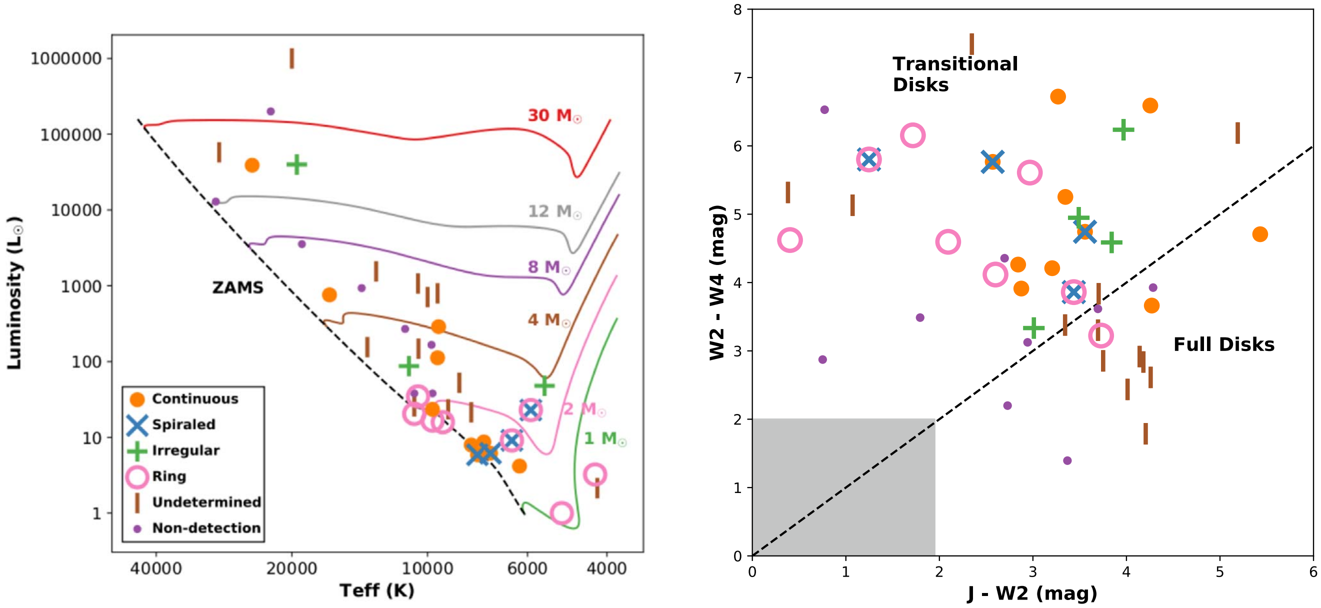

Figure 11. HR diagram (left) and color–color diagram (right) of this work's entire sample. Each target is marked by its apparent polarized light disk structure described in Section 4.2. HR diagram includes pre-main-sequence mass tracks (colored lines) and the zero-age main sequence (ZAMS) assuming solar-metallicity mass tracks from Bressan et al. (2012). Note that FU Ori is not plotted on the HR diagram as the $T_{\rm eff}$ temperature is unknown.

brightness from the target star. We measured the local star density by using the number of stars per half magnitude within 1 deg of the target from the 2MASS catalog. We then calculated the probability that a background star would be located within the projected distance of the target. We found that 22 of the 24 point sources are likely not background stars within 3σ. Two point sources found around V921 Sco are less than a 2σ probability not being background stars. Based on the likelihood that all of the point-source companions are gravitationally bound; for the purposes of this work we will assume that all of the 24 point

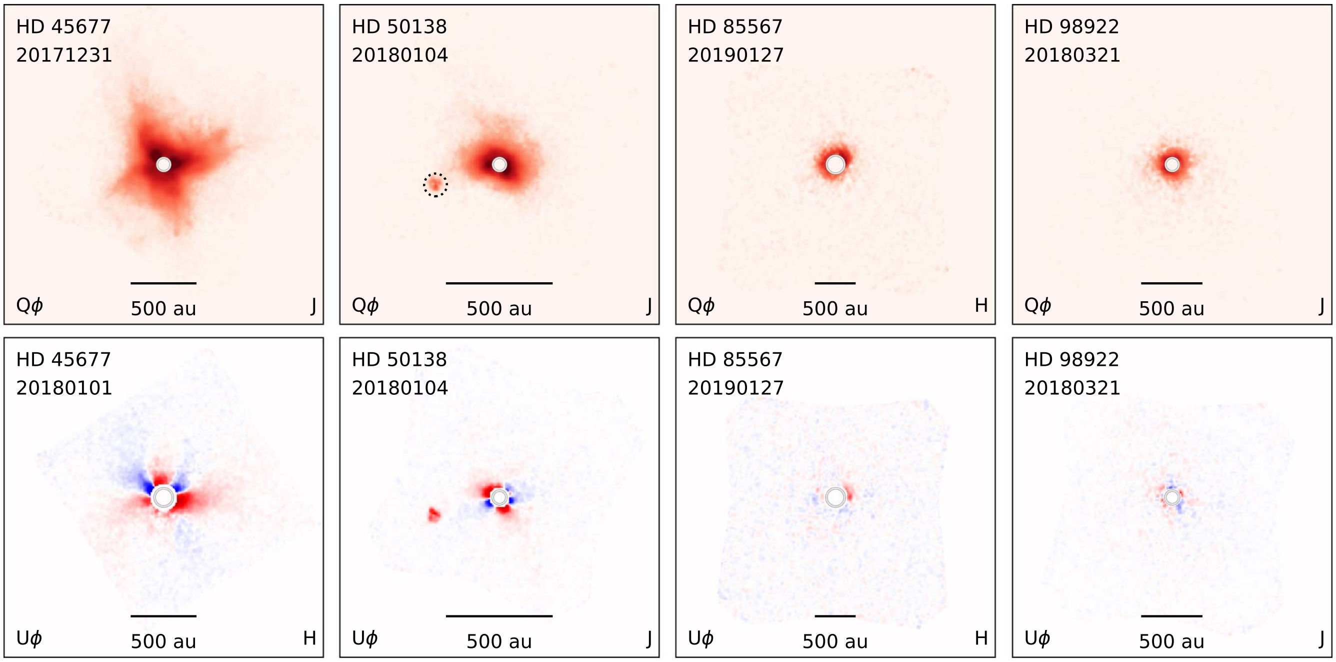

Figure 12. Q_ϕ and U_ϕ images of targets that have previously been classified as FS CMa. The image scale is log and chosen to show target structure. See the figure set appearing on the online version of this work (Figure 2) for target specific color bars. The point sources in the FOV are labeled with a dashed black circle in Q_ϕ images. The name of the target and the epoch in YYYYMMDD format can be found in the upper left of each image. The type of polarized image (Q_ϕ or U_ϕ), the 1" scale and the size in au, and the photometry band (J or H) can be found along the bottom of each subimage. In U_ϕ images, red is positive and blue is negative flux.

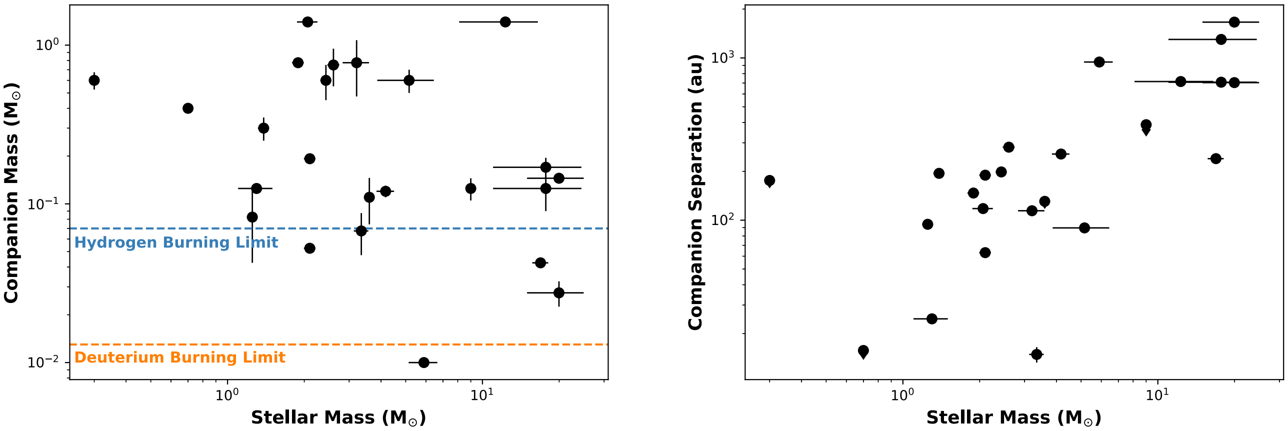

Figure 13. Comparison of the stellar mass and estimated companion mass (left) and of the stellar mass and projected companion separation (right). For the companion masses, we denote the boundary between brown dwarfs and stars (hydrogen burning limit: blue) and denote the boundary between planets and brown dwarfs (deuterium burning limit: orange).

sources are binaries. However, future follow-up observations, especially V921 Sco, are needed.

We estimated the masses of each of the companions using the age of the system and the companions measured flux and extrapolated the mass from evolutionary models from Baraffe et al. (2015) for masses $>0.01\,M_\odot$ and Phillips et al. (2020) for masses $<0.01\,M_\odot$. We estimated the mass uncertainties using the uncertainty in the systems age and flux. We note that some of our targets have ages less than 0.5 Myr, which is younger than the youngest age by Baraffe et al. (2015). In these cases, we estimated their mass based on the youngest age in the Baraffe et al. (2015) models to give an idea of their mass but note these masses should not be used for future analysis as they are not reliable. Estimated masses are tabulated in Table 6 located in the appendix.

We compare the estimated companion mass and the projected companion separation to the stellar mass, as shown in Figure 13. Of our 24 point sources, one point source around V1295 Aql has a mass consistent with a super Jupiter, four have masses consistent with brown dwarf masses (HD 101412, HD 158643, MWC 297, and V921 Sco), 12 systems have companions with masses consistent with M dwarfs (0.08–0.57 $M_\odot$), and seven have masses $>0.57\,M_\odot$. Further, we note that more massive stellar objects ($>6\,M_\odot$) have larger projected separations due to these objects being more distant. For these objects with separations >1000 au, future observations are necessary to determine if these objects are comoving and if they are gravitationally bound.

4.5. Possible Nonconcentric Reflection Nebulae

Two targets, MWC 147 and TY CrA, have polarized flux that is adjacent to the target, as shown in Figure 14. The flux plotted is flux that is 1σ per pixel above the noise in the image.

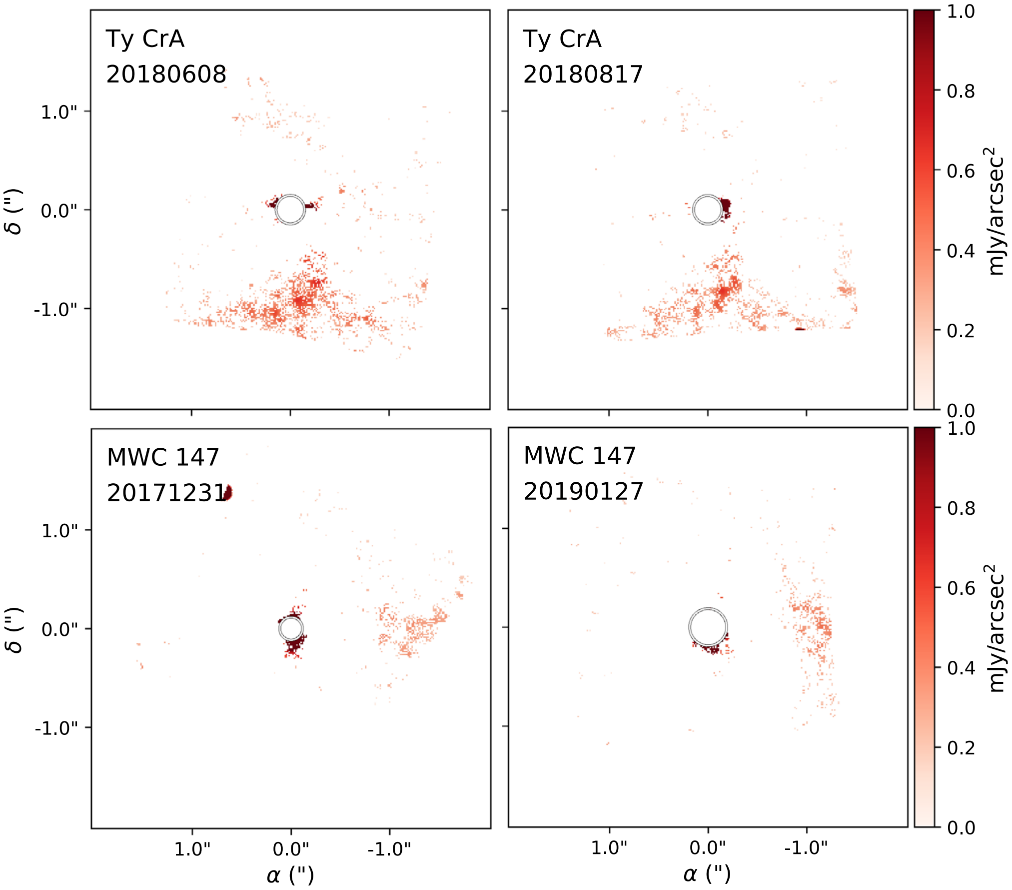

Figure 14. Target adjacent polarized flux of TY CrA (top row) and MWC 147 (bottom row) for two different epochs. Both targets have point sources (dashed circles) close to the inner working angle (solid circle). The companion and flux $<1\sigma$ are masked in the images. The flux is in mJy $''^{-2}$.

Both targets are known to be associated with reflection nebulae; thus the flux is likely material that is part of the larger reflection nebulae. We also note that the flux may be an instrumental effect due to known issues with flat-fielding (see Section 3.2). However, this explanation is unlikely as the features appear in the same location over multiple epochs and multiple bands, and no other sources show these features taken on the same night.

4.6. Systems with Stellar Masses >8 $M_\odot$

Six of our systems have stellar masses $>8\ M_\odot$ including Hen 3-365, Hen 3-1330, MWC 166, MWC 297, V921 Sco, and WRAY 15-535. We do not detect polarized light around two of the six systems (Hen 3-1330 and MWC 166), and we classified the morphology of the rest as one irregular (Hen 3-365), one continuous (MWC 297), and two undetermined (V921 Sco, WRAY 15-535). Several of these objects have conflicting classifications between young stellar objects (YSOs) and post -main-sequence stars. Hen 3-365 is discussed by Laws et al. (2020) who noted that it is inconsistent with being a massive supergiant due to the large H I column density, but parallax distances are consistent with being an evolved star (Oudmaijer et al. 1998; Maravelias et al. 2018). Hen 3-1330 has previously been classified as a WR+O binary system (Richardson et al. 2011). V921 Sco has been classified as both a supergiant and as a Herbig Be star (Kreplin et al. 2020). WRAY 15-535 has been classified as a supergiant B[e] star (Domiciano de Souza et al. 2007). Finally, previous work investigating MWC 166 and MWC 297 has shown that they are consistent with being Herbig Ae/Be stars (Manoj et al. 2007; Wichittanakom et al. 2020). We leave the polarized light investigations of these individual targets to future work.

4.7. Scattered Light Diagnostics

We calculate the total amount of Q_ϕ flux within the image relative to the stellar flux Fstar. To mitigate noise being added into the images, we sum all of the Q_ϕ light between the IWA of the target and where the radial profile of the Q_ϕ is within 3σ of zero flux using error propagation from the bootstrapped images discussed in Section 3.3. The summed Q_ϕ flux is then divided by the flux of the star using the 2MASS *J*- and *H*-band flux. The Q_ϕ/Fstar ratio can be found in the appendix in Table 5. We note that this simplified methodology does not account for the r^2 flux loss. However, this method can easily be applied to our entire sample and is not dependent on knowing the disk geometry (i.e., disk inclination), which is not possible for some systems (i.e., unclassified, irregular; see Section 4.2). As there are multiple epochs of some targets, we will use the weighted average of Q_ϕ/Fstar ratio for all analysis.

We first compare the Q_ϕ/Fstar ratio to the color–color diagram shown in Figure 15, which we utilized for our target selection described in Section 2. The size of the circle corresponds to the Q_ϕ/Fstar ratio on a logarithmic scale. We find that the targets with the largest Q_ϕ/Fstar ratio are commonly found in the middle of the color–color plot between $3<$ W2–W4 <6 mag and $2 <$ J–W2 <4 mag. This region coincides with the transitional disk region as outlined in

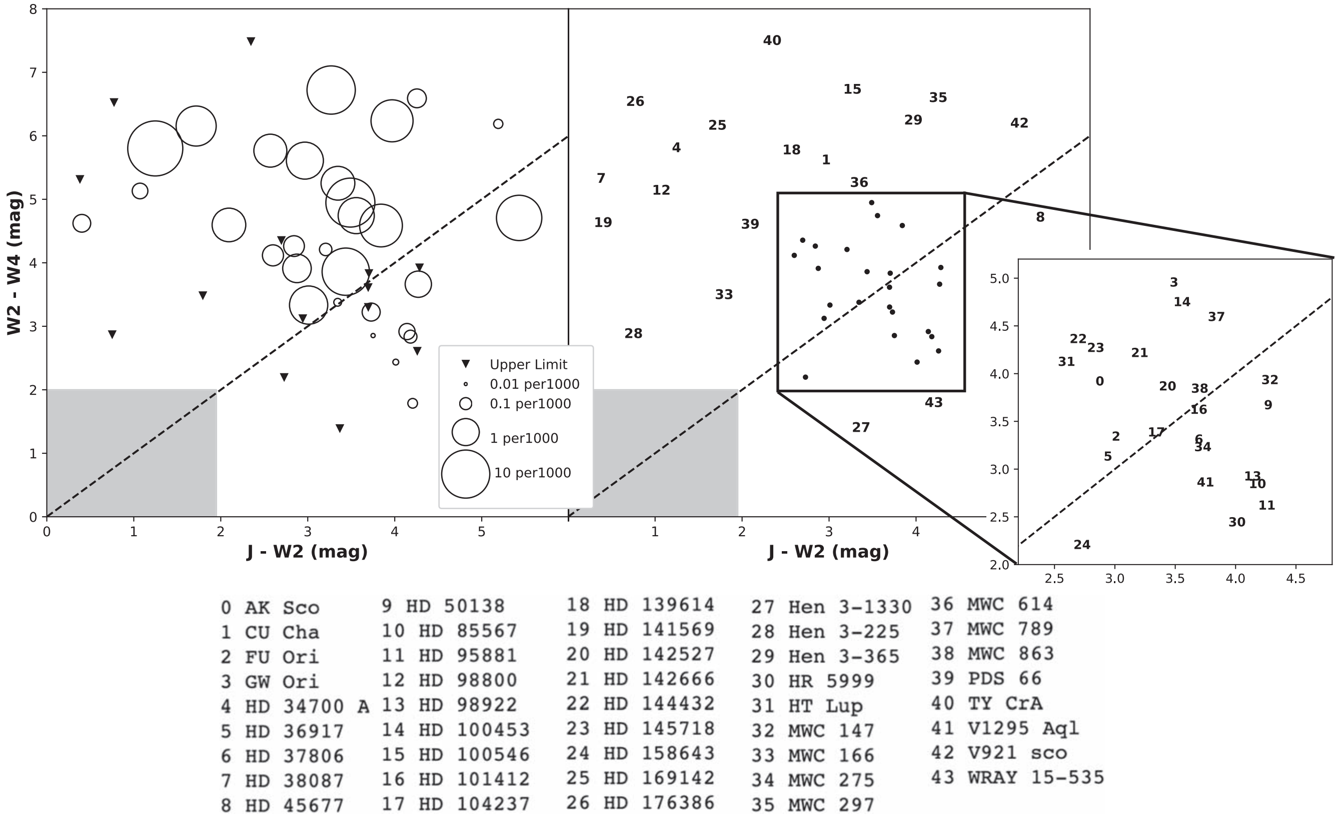

0	AK Sco	9	HD 50138	18	HD 139614	27	Hen 3-1330	36	MWC 614
1	CU Cha	10	HD 85567	19	HD 141569	28	Hen 3-225	37	MWC 789
2	FU Ori	11	HD 95881	20	HD 142527	29	Hen 3-365	38	MWC 863
3	GW Ori	12	HD 98800	21	HD 142666	30	HR 5999	39	PDS 66
4	HD 34700 A	13	HD 98922	22	HD 144432	31	HT Lup	40	TY CrA
5	HD 36917	14	HD 100453	23	HD 145718	32	MWC 147	41	V1295 Aql
6	HD 37806	15	HD 100546	24	HD 158643	33	MWC 166	42	V921 sco
7	HD 38087	16	HD 101412	25	HD 169142	34	MWC 275	43	WRAY 15-535
8	HD 45677	17	HD 104237	26	HD 176386	35	MWC 297		

Figure 15. Infrared color–color plot (left) of the targets where the size of the circle corresponds to the magnitude of the Q_ϕ/Fstar ratio. Note that the size of the circles is logarithmic. The color–color diagram is the same as that shown in Figure 1 where colors are using 2MASS *J*-band magnitudes and WISE 2 (4.6 μm) and 4 (22 μm) bands representing near-infrared excess (J–W2) and mid-infrared excess (W2–W4). The dashed line represents a flat spectrum SED. The gray shaded region marks objects with no near-infrared or mid-infrared excess. The color–color diagram (right) labels each target with the corresponding number and target name on the bottom of the figure. The Q_ϕ/Fstar ratios plotted are the weighted average for each target. The individual Q_ϕ/Fstar values can be found in Table 2.

Figure 1. Low and nondetected Q_ϕ/Fstar ratios are scattered throughout the diagram but have a higher concentration at the bottom with W2–W4 <3 mag. This lower-right portion of the diagram coincides with the location of the full disks shown in Figure 1. Interpretation of these results will be discussed in Section 6.

5. Scattered Light Trends

We next compare the total amount of summed scattered light per stellar flux, Q_ϕ/Fstar, to disk and stellar parameters to find which parameters affect the amount of scattered light flux. Due to the diverse nature of our sample, there are some very-high-mass and very-low-mass stars. Here, we restrict our sample to only include stars between A-type stars ($>1.4\,M_\odot$) up to stars that will produce supernovae ($<8\,M_\odot$). When we have this restriction, we have a sample size of 33 targets that are also all in the Vioque et al. (2018) sample, which provides a common source of temperatures, ages, and masses. In this section we will only analyze these 33 targets.

We will compare our subsample of 33 targets to their binarity, defined as either an outer binary where the stellar/substellar companion can be directly imaged in our sample (separation >0.″12) or an inner binary (separation <0.″12). Binarity is determined using high-contrast imaging (see Section 3.4) or is previously determined in the literature using spectroscopy, imaging, or interferometry. For the 33 targets in this sample, we are able to detect binaries with masses down to brown dwarfs ($0.075\,M_\odot$) at a separation of 0.″2. There are three exceptions, HD 142527, HD 142666, and HD 158643, which did not have sufficient field rotation to determine contrast upper limits at 0.″2. However, given the depth and that all of our binary targets identifiable in the intensity frame without the aid of ADI, we expect a similar sensitivity for these targets as well. We note that the statistics of inner binaries is not complete as we are dependent on previous studies, and it can be notoriously difficult to detect Doppler shift of binaries in YSOs. Additionally, our analysis is not complete for outer binaries with separations larger than the FOV (separation >1.″9) and would not be detected by our survey.

Lastly, we investigate the commonly used Meeus Group I and Group II categorization (Meeus et al. 2001) of Herbig Ae/Be SEDs. Group I disks have much larger far-infrared fluxes than Group II disks, and this classification is a version of the W2–W4 color but with only two categories. Here, we calibrated our WISE-based Group I and Group II classification (see Table 2) using the previous classification by Guzmán-Díaz et al. (2020), which has 29 of our targets in their Herbig Ae/Be sample.

5.1. Infrared Colors

We first compare the Q_ϕ/Fstar ratio to the W2–W4 color shown in Figure 16. We find that bluer targets are more likely to have lower Q_ϕ/Fstar ratios than redder targets. By our group definition above, Group II targets are more likely to have lower Q_ϕ/Fstar ratios, while Group I targets are more likely to have higher Q_ϕ/Fstar ratios. While there is a positive trend between

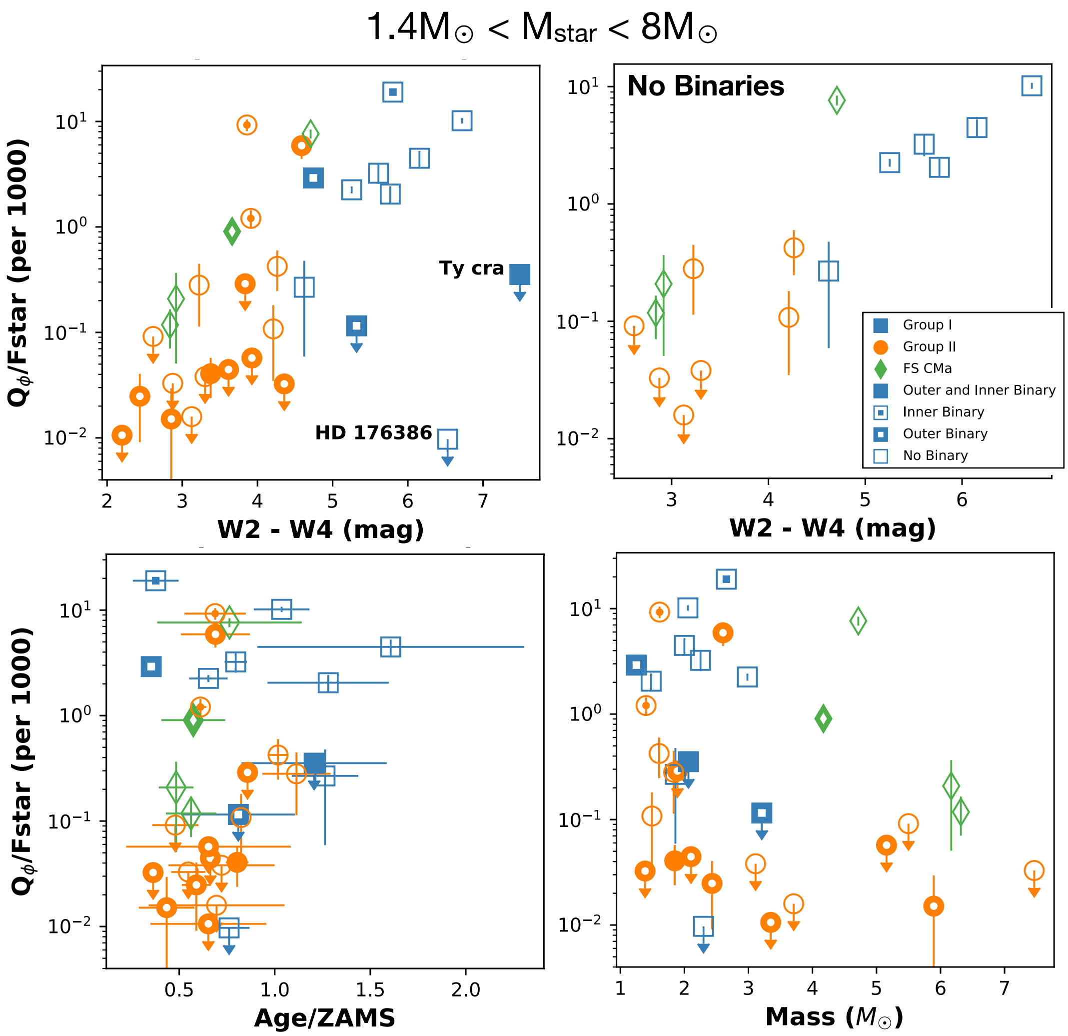

Figure 16. 33 targets with 1.4 $M_\odot$< stellar Mass <8 $M_\odot$ comparing the Q_ϕ/Fstar ratio to the system parameters of WISE 2 (W2, 4.6 μm)–WISE 4 (W4, 22 μm) color (upper right), W2–W4 color of only nonbinary systems (upper left), system age/ZAMS age (bottom left), and stellar mass (bottom right). The target shapes and colors refer to their classification (Group I-blue squares, Group II-orange circles, FS CMa-green diamonds) and the shape filling refers to the binarity (filled shapes: inner and outer binary; edge filled: outer binary; inner filled: inner binary; no filling: no binary). Outer binaries are exterior to the IWA and in the FOV as discussed in Section 3.4. Inner binaries are spectroscopic binaries from the literature. Error bars are plotted under the symbols with down pointing errors indicating the 2σ upper limit uncertainty.

the Q_ϕ/Fstar ratio and the W2–W4 color, there is a large spread of values in the trend especially noting the logarithmic plots in Figure 16. We attribute this large spread due to the presence of binaries. When the binaries are removed from the sample, as shown in the upper right in Figure 16, there is not as significant of a spread in values. This suggests that binarity complicates the correlation between polarized flux from the disk versus infrared color. Very bright binaries can make it difficult to remove the SIP, as discussed in Section 3, possibly resulting in a larger spread in Q_ϕ/Fstar ratio values. However, this is unlikely to be the main cause of the spread as the majority of binaries in these systems are not bright enough to leave the quadrupole residual in Q_ϕ and U_ϕ .

There are two clear exceptions to this trend, TY CrA and HD 176386. Both of these targets have no detected Q_ϕ/Fstar ratios; yet both are very red (W2–W4 >6 mag). TY CrA and HD 176386 are both located in an extended reflection nebulae. Images from unWISE of TY CrA exhibit extended emission offset from TY CrA (Lang et al. 2016). Also, HD 176386 is most likely blended with CrA-54 in WISE bands, where CrA-54 is a K7 star that is known to host a disk (Cazzoletti et al. 2019). Thus we conclude that the W2–W4 color for TY CrA and HD 176386 are likely contaminated from their surrounding environment (reflection nebulae, close-by stars, dust clumps), not originating from the protoplanetary disk dust around these stars. However, we lack observations of adequate spatial resolution to provide accurate WISE-band fluxes; thus we will keep these targets in our analysis but label them as suspicious WISE fluxes.

5.2. Age

We next compare the summed Q_ϕ/Fstar flux to the ages of the systems. Stars will evolve toward the zero-age main sequence (ZAMS) at different rates with 8 $M_\odot$ stars evolving much quicker than 1.4 $M_\odot$ stars. Thus we plot the ratio of the current age of the stars divided by the target ZAMS for a given estimated stellar mass, as shown at the bottom left of Figure 16. For reference, the ZAMS is also plotted on an HR diagram for the sample in Figure 11. There are no systems with Q_ϕ/Fstar ratios <0.2 that are on the main sequence (>1.0 Age/ZAMS). We do not see a correlation between the system age/ZAMS and the Q_ϕ/Fstar ratio.

5.3. Stellar Mass

Finally, we compare the stellar mass to the ratio of Q_ϕ/Fstar shown at the bottom right of Figure 16. We find that the less massive stars have the largest Q_ϕ/Fstar. The one key result is looking at systems with stellar masses between $4 < M_{\rm star} < 8\,M_\odot$, where only five systems have significantly detected Q_ϕ/Fstar. Four of these five systems are also classified as FS CMa stars. We will discuss this point further in Section 6.6.

6. Discussion

6.1. Ringed Systems and Stellar Mass Dependence

We found that, in our sample, protoplanetary disks hosting ringed systems only occur in systems with stellar masses $<3\,M_\odot$ (see Section 4). There are several potential causes that could explain this trend. First, we note that dust ringed systems have largely been theorized to exist due to the formation of exoplanets creating gaps in-between these dusty rings. Recent evidence for this theory has been provided in the case of PDS 70b,c (Keppler et al. 2018). One explanation is that the physical scenarios that make it possible for exoplanets to form visible rings at lower stellar masses ($<3\,M_\odot$) do not exist for higher-stellar-mass systems. One possibility is the increased binarity for stellar masses $>3\,M_\odot$ disrupts the formation of rings and gaps, which was similarly observed for millimeter dust grains as part of the DSHARP sample (Kurtovic et al. 2018). However, in our sample we see the same fraction of binaries around more massive stars (42% for $3\,M_\odot <$ stellar mass $<8\,M_\odot$) than we do around lower-mass stars (40% for Stellar Mass $<3\,M_\odot$) though we are not complete to inner and outer binaries as noted in Section 5. Second, the temperature of the higher-mass disks may prevent them from forming rings and gaps. Disks around higher-mass stars may be hotter, which can prevent the most volatile ice species, like CO, from freezing out onto dust grains, as found recently in a comparison of carbon depletion in T Tauri versus Herbig AeBe disks (van der Marel et al. 2021; Sturm et al. 2022). If the dust rings are created by the accumulation of millimeter-sized grains at the edges of gaps, which may in turn be carved by planets, reduced amounts of CO or CO_2 ice in the warmer disks could inhibit planetesimal formation or grain growth. This could inhibit outer disk ring formation for the higher-mass disks. Garufi et al. (2018) found that polarized light rings only appeared around older stars (>5 Myr); thus what we may be observing is that stellar systems with masses $>3\,M_\odot$ do not have the time to develop polarized light rings before the dust has been removed from the system. Also, theoretical predictions suggest that the mass of a planet needed to open a gap in a disk is proportional to the mass of the star (see Equation (1) in Matsumura & Pudritz 2003). Thus the lack of gaps could be representative of more massive planets being needed to open up gaps around more massive stars.

Finally, the lack of detected ringed systems for stellar masses $<3\,M_\odot$ could be an observational bias. In our sample, more massive targets are more likely to be more distant. Thus these more distant objects may host ringed structures but are located inside the IWA of our observations. Of the 20 systems with stellar masses $>3\,M_\odot$ (see Figure 11), all rings in the two systems with stellar masses $<3\,M_\odot$ could be detected, and an additional 11 systems are close enough that at least one ring could be detected. Our sample has a dust ring occurrence rate of 30% for systems with $<3\,M_\odot$ stars; thus we would expect to detect at least one system with stellar mass $>3\,M_\odot$ hosting rings. However, the detectability of rings around more massive systems is complicated because the central stars are also more luminous, increasing the outer disk brightness. Therefore ringed structures around systems with masses $<3\,M_\odot$ that are too dim to be detected by our imaging surveys, such as those found around MWC 275 (330 au; Rich et al. 2019) and CU Cha (341 au; Ginski et al. 2016), would be brighter and detectable around more luminous systems. If we assume the distance of the furthest known ring (341 au), we could detect such a ring around 15 of 20 systems with stellar masses $>3\,M_\odot$. Our survey is the first survey to search for trends in protoplanetary disks with stellar masses $>3\,M_\odot$; thus future work needs to verify these findings and search for massive systems that host ringed and gaped structures.

6.2. Polarized Flux and Infrared Color

We find a correlation between the polarized flux and the infrared colors, as shown for the entire sample in Figure 15. This trend replicates previous studies by Garufi et al. (2017, 2020), which found a similar correlation. For the entire sample, we find that objects associated with full disks are more likely to have a lower Q_ϕ/Fstar ratio, as shown in Figure 15. The lower Q_ϕ/Fstar ratio is expected as full disks are thought to self-shadow, causing the outer portions of the disk imaged with GPI to be dimmer in polarized light as compared to transitional disks where self-shadowing is not occurring.

A similar trend can be seen for our limited Herbig Ae/Be sample discussed in Section 5. The strong infrared flux of Group I objects has often been interpreted as due to strong disk flaring but could also be due to disk cavity, in either case leading to easily detected scattered light disk flux (Maaskant et al. 2013; Garufi et al. 2017, 2018). The bluer Group II objects can be explained either by strong self-shadowing by the inner disk or a flatter geometry due to dust growth/settling (e.g., Muro-Arena et al. 2018). This would broadly correspond to larger scattered light flux from Group I objects and less from Group II objects. Our observations shown in Figure 16 broadly replicate this trend though there is a large spread in values. This is primarily due to the presence of binaries. Further, we observe very few binaries that are in redder objects (Group I for Herbig's) and most binaries in our sample are associated with bluer objects, as shown in Figure 16. This strongly suggests that a system hosting a binary plays a significant role in the Group I versus Group II classification. One potential cause is that the presence of binaries truncate the outer disks causing systems with binaries to have less polarized fluxes or not be resolved. This would match with previous studies suggesting that Group I and Group II systems are two distinct evolutionary pathways (Maaskant et al. 2013; Garufi et al. 2018).

6.3. Polarized Flux and Age

We observe a lack of systems with ages in the main sequence (>1.0 Age/ZAMS) and low Q_ϕ/Fstar ratios, as discussed in Section 5. This could be an indicator that systems with low Q_ϕ/Fstar ratios and older ages (>1.0 Age/ZAMS) do not have sufficient infrared excess and are thus not in our sample. However, the brightest systems with large Q_ϕ/Fstar ratios may have long-lived disks. This is similar to the conclusion found by Garufi et al. (2018), where the most massive disks are long-lived and easily observed in polarized light to older ages. Next, we do not find the correlation between Q_ϕ/Fstar and age, which had previously been observed by Garufi et al. (2018). However, our sample contains a larger range in stellar mass of 0.3–20 $M_\odot$, whereas the Garufi et al. (2018) study only contained targets with stellar masses $<3\,M_\odot$. Thus, the correlation between polarized light and age may not be present for higher-mass stars. Finally, age results are difficult to interpret for more massive stars due to the lack of intermediate-mass T Tauri stars in our sample (see Section 2). Future work is needed to include intermediate-mass T Tauri stars in polarized light imaging surveys to assess age trends in Herbig Ae/Be systems.

6.4. Polarized Flux and Binarity

We find that only 5 of the 12 systems with stellar masses between $4\ M_\odot < M_{\rm star} < 8\,M_\odot$ have significantly detected Q_ϕ/Fstar ratios. There are four possible explanations for this trend. First, our more massive stars tend to be further away; thus, we may not be resolving as much of the polarization flux compared to closer systems. Second, these more massive stars tend to have more outer binaries (5 of 12) than less massive systems ($<4\,M_\odot$). These binaries could be truncating or stripping the disks from the central star. The lack of polarized light may be caused by stellar evolution, where the quickly evolving bright star photoevaporates the disks so they are no longer visible. Finally, the systems may host large disks that our imaging would resolve. However, no polarized light is detected because the inner disk shadows the outer disk. This mechanism has previously been invoked to explain nongaped protoplanetary disks having little polarized light detected (Garufi et al. 2017; Muro-Arena et al. 2018).

6.5. Point Sources in Literature

We compare our point-source findings to those found in the literature. We limit our discussion to the substellar mass companions and notable stellar companions. Our survey has imaged five substellar point sources (V921 Sco, HD 158643, MWC 297, HD 101412, and V1295 Aql). We found two companions around V921 Sco at 0."5 (0.03 $M_\odot$) and 1."1 (0.15 $M_\odot$). The first companion with a mass consistent with a brown dwarf at 0."5 was previously discovered by Ubeira-Gabellini et al. (2019) with a similar mass estimate (0.06 $M_\odot$) but has not previously been confirmed until this work. They did not observe the second companion at 1."1; however this is expected as the second companion is located outside of the FOV of Ubeira-Gabellini et al. (2019) images. The brown dwarf object (0.07 $M_\odot$) HD 158643 has not been directly imaged previously. However, Kervella et al. (2019) measured a variation in the proper motion of the system consistent with an object with a mass of 0.05 $M_\odot$ normalized to a separation of 1 au. These values are potentially consistent, but further analysis is necessary. Ubeira-Gabellini et al. (2020) previously confirmed that MWC 297 B was comoving and measured the companion mass to be $0.25^{+0.25}_{-0.15}\,M_\odot$. This is much larger than our estimated mass of 0.03 $M_\odot$. However, they were also able to measure a local high extinction of $A_V \sim 11.9$ mag from the spectral slope of the planet, which is sufficient to match our findings. Finally, there is no known previous discovery of the planetary mass companion around V1295 Aql or a brown dwarf companion around HD 101412. Follow-up observations to confirm that these objects are comoving is necessary.

Ty CrA is a known quadrupal system with Chauvin et al. (2003) observing the fourth stellar companion around Ty CrA. The Chauvin et al. (2003) work was unable to verify if the object was comoving. Given the 16 year difference between our observations and Chauvin et al. (2003) observations and assuming the proper motion of Ty CrA, we find that if the fourth component was not comoving, the object would have moved by 0."52, while we measure a positional difference of 0."21. Given the large timescale and that the fourth component of Ty CrA is at a projected separation of ∼18 au, it is likely we are observing the orbital motion of the fourth component of Ty CrA. However, confirmation of the object being bound is necessary given the systems complex orbital dynamics.

6.6. Classification of FS CMa stars

For the four systems that are FS CMa candidates in our sample, HD 45677, HD 50138, HD 85567, and HD 98922, we observe polarized flux at large projected distances (>200 au), as shown in Figure 12. Additionally, these polarized signals are bright, and in the case of HD 45677 and HD 50138 there is significant U_ϕ polarized flux suggesting multiple scattering events due to the optically thick nature of the material.

Previous studies have detected extended structures around B [e] stars via H-alpha (Marston & McCollum 2008; Liimets et al. 2022). These structures are typically shell-like or indicative of bipolar outflows. We do not observe similar structures around our four FS CMa candidates, which appear to be closer to typical protoplanetary disk structures. However, previous studies were at a larger spatial scale (>1′) and emission, while our observations are at smaller spatial scales and from a polarized source. Finally, our targets have a lower mass than those studied by Marston & McCollum (2008) and Liimets et al. (2022).

Stars that exhibit the B[e] phenomenon are a heterogeneous group that include pre-main-sequence, main-sequence, and evolved systems. Additionally, many of these stars exhibit similar features making classification difficult. FS CMa as defined by Miroshnichenko et al. (2007) hosts emission-line spectra containing hydrogen lines; large infrared excess that peaks at 10–30 μm, located outside of a star-forming region; and if it has a secondary companion it is either fainter and cooler than the primary or degenerate. However, even given these parameters, distinguishing between B[e] classifications can be difficult. For example, a thorough investigation by Varga et al. (2019), which studied HD 50138, concluded that the evolutionary state of HD 50138 could not be unambiguously determined through mid-infrared spectroscopy. We conclude that the structures observed around the FS CMa candidate stars in our Q_ϕ and U_ϕ images are more similar to the expected structures of protoplanetary disks rather than outflow from FS CMa or another type of evolved star. Future investigations into the resolved circumstellar material around stars are necessary including resolved ALMA observations to test the kinematics of the gas in the systems. The classification of these systems to be protoplanetary is extremely important as they represent four of the five systems with $4\,M_\odot < M_{\rm star} < 8\,M_\odot$ in our sample that have detected scattered light flux.

7. Summary

We have presented the Gemini-LIGHTS survey, which observed 44 bright Herbig Ae/Be stars and T Tauri stars with the GPI instrument at Gemini South. We constructed our sample based on their near- and mid-infrared colors selecting a number of transitional, pre-transitional, and full disks in order to create an unbiased sample. Importantly, we did not select against unequal mass binaries with moderate separations. Observations of these 44 targets were taken in *J* and *H* bands utilizing high-contrast polarized imagery. Our selection criteria facilitate an unbiased approach to studying bright Herbig Ae/Be and T Tauri stars that does not favor famous targets with large disks (>100 au). We discussed how we uniformly reduced and analyzed the 70 epochs of observations that are part of the sample using the GPI DRP pipeline along with our own Python wrapper. We discussed improvements to finding centers of images with bright companions and improvements in removing SIP.

Within our sample of 44 targets, we found several significant trends:

1. We detect scattered light signatures around 80% of our 44 targets.
2. Systems with large separation binaries are more likely to have bluer mid-infrared colors (Group II), and these systems are more likely to have no detectable Q_ϕ/Fstar fluxes.
3. We find that all ringed classified systems have stellar masses $<3\,M_\odot$, potentially indicating that if the disk rings arise from planet formation, the planet formation process or disk evolution is different around more massive stars.
4. We find a similar infrared (WISE 2–WISE 4) correlation with Q_ϕ/Fstar identified by Garufi et al. (2017). We find a large spread in values primarily due to binary systems as the trend is much tighter when binaries are removed.
5. Four of five of our targets with $4\,M_\odot < M_{\rm star} < 8\,M_\odot$ for which we have detected scattered light flux are also classified as FS CMa (HD 45677, HD 50138, HD 85567, and HD 98922). Due to the large radial extent of the polarized flux in the images (>200 au), we conclude that these objects are likely young systems.
6. We detect 24 point sources consistent with being star companions. We find 1 point source around V1295 Aql that is consistent with a super-Jupiter mass and 3 point sources consistent with brown dwarf masses. We confirm the existence of two brown dwarf candidates (V921 Sco, HD 158643) from previous direct imaging and proper motion discoveries. We find one brown dwarf candidate HD 101412, which had previously not been observed before.

Thanks to Christian Ginski for their collaboration on defining the FITS header standard for high-contrast scattered light imaging. We would also like to thank Bruce Macintosh, Fredrik Rantakyro, Marshall Perrin, Max Millar-Blanchaer, Tom Esposito, Robert De Rosa, Jeffrey Chilcote, and René Rutten for their help on this survey. E.A.R. and J.D.M. acknowledge support from NSF AST 1830728. A.A. acknowledges support from NSF AST-1311698. S.K. acknowledges support from an ERC Consolidator Grant (Grant Agreement ID 101003096). L.P. gratefully acknowledges support by the ANID BASAL projects ACE210002 and FB210003, and by ANID—Millennium Science Initiative Program—NCN19_171. We thank the anonymous referee for feedback that helped to improve this paper. This work has made use of data from the European Space Agency (ESA) mission Gaia (https://www.cosmos.esa.int/gaia), processed by the Gaia Data Processing and Analysis Consortium (DPAC; https://www.cosmos.esa.int/web/gaia/dpac/consortium). Funding for the DPAC has been provided by national institutions, in particular the institutions participating in the Gaia Multilateral Agreement.

This work is based on observations obtained at the international Gemini Observatory, a program of NSFs NOIRLab, which is managed by the Association of Universities for Research in Astronomy (AURA) under a cooperative agreement with the National Science Foundation on behalf of the Gemini Observatory partnership: the National Science Foundation (United States), National Research Council (Canada), Agencia Nacional de Investigación y Desarrollo (Chile), Ministerio de Ciencia, Tecnología e Innovación (Argentina), Ministério da Ciência, Tecnologia, Inovações e Comunicações (Brazil), and Korea Astronomy and Space Science Institute (Republic of Korea). List of program ID's where the data were obtained: GS-2017A-LP-12, GS-2017B-LP-12, GS-2018A-LP-12, GS-2018B-LP-12, GS-2015A-C-1, GS-2016B-DD-5, GS-2015B-Q-501, GS-2014B-Q-503, GS-2018A-FT-101-17, GS-2018A-FT-101-15, GS-2018A-FT-101-5, GS-2014A-SV-414-14, GS-2014A-SV-414-8, GS-2014A-SV-406-5, GS-2017B-Q-500-16, GS-2014A-SV-412, and GS-2015A-Q-49.

Appendix A
Target Properties

In this section, we provide the target parameters, observation log, and calculated values used in this work. Table 1 lists all of the targets, HD names, their coordinates, and their GAIA distances. Table 2 lists the targets of the Gemini-LIGHTS sample along with target system properties such as the stellar mass, age, effective temperature, and luminosity. The photometry used in this work is listed in Table 3.

Table 4 lists each of the 70 observational epochs observed as part of the Gemini-LIGHTs sample. The table lists each target, filter, date of observation, length of image exposure, and number of frames. Additionally, the table lists the average % polarization that was removed during the reduction. Note that this value is a combination of SIP and for small values of % polarization, the polarization will be dominated by the instrumental polarization.

Table 5 lists the measured Q_ϕ/Fstar ratio for every observed epoch. A description of how Q_ϕ/Fstar is calculated can be found in Section 5. Additionally, the 5σ upper limit of potential point sources detected at a separation of $0\rlap{.}''2$ is listed in Table 5. Details on the ADI reduction and analysis can be found in Section 3.4. Table 6 lists the point sources detected in the Gemini-LIGHTS sample.

Table 1
Gemini-LIGHTS Target Sample

Target	HD Name	2MASS Name	R.A. (°)	Decl. Decl. (°)	Distance (pc)
AK Sco	HD 152404	16544485-3653185	253.6868708	−36.8887086	139.8 ± 0.6
CU Cha	HD 97048	11080329-7739174	167.013825	−77.6548583	184.4 ± 0.8
FU Ori	⋯	05452235+0904123	86.3431986	9.0700691	407.5 ± 3.0
GW Ori	HD 244138	05290838+1152126	82.2849625	11.8701944	408.0 ± 10.4
HD 34700 A	HD 34700	05194140+0538428	79.9225333	5.6452111	350.5 ± 2.5
HD 36917	HD 36917	05344698-0534145	83.6957719	−5.5707229	450.4 ± 11.3
HD 37806	HD 37806	05410229-0243006	85.2595665	−2.7168744	401.6 ± 4.4
HD 38087	HD 38087	05430057-0218454	85.752413	−2.3125911	377.0 ± 5.4
HD 45677	HD 45677	06281742-1303109	97.0726019	−13.0530934	572.1 ± 14.6
HD 50138	HD 50138	06513340-0657592	102.8891461	−6.9664934	351.0 ± 5.7
HD 85567	HD 85567	09502853-6058029	147.6188579	−60.9674551	1047.4 ± 18.0
HD 95881	HD 95881	11015764-7130484	165.4900393	−71.5134176	1109.9 ± 24.3
HD 98800	HD 98800	11220530-2446393	170.5215893	−24.7778864	42.1 ± 1.0
HD 98922	HD 98922	11223166-5322114	170.631975	−53.3698472	650.9 ± 8.8
HD 100453	HD100453	11330559-5419285	173.2730745	−54.3246148	103.8 ± 0.2
HD 100546	HD100546	11332542-7011412	173.3558188	−70.1947875	108.1 ± 0.4
HD 101412	HD 101412	11394445-6010278	174.9352141	−60.1743876	412.2 ± 2.5
HD 104237	HD 104237	12000511-7811346	180.0211875	−78.1929333	106.6 ± 0.5
HD 139614	HD 139614	15404638-4229536	235.1931708	−42.4983306	133.6 ± 0.5
HD 141569	HD 141569	15495775-0355162	237.4905224	−3.9213039	111.6 ± 0.4
HD 142527	HD 142527	15564188-4219232	239.1744971	−42.323228	159.3 ± 0.7
HD 142666	HD 142666	15564002-2201400	239.1667625	−22.0277806	146.3 ± 0.5
HD 144432	HD 144432	16065795-2743094	241.7414345	−27.7195047	154.8 ± 0.6
HD 145718	HD 145718	16131158-2229066	243.2982588	−22.4853188	154.7 ± 0.5
HD 158643	HD 158643	17312497-2357453	262.8540017	−23.9627733	125.7 ± 1.7
HD 169142	HD 169142	18242978-2946492	276.1240709	−29.7805404	114.9 ± 0.4
HD 176386	HD 176386	19013892-3653264	285.4122394	−36.890856	155.1 ± 0.7
Hen 3-1330	HD 326823	17065390-4236397	256.7246196	−42.6110631	1445.2 ± 40.0
Hen 3-225	HD 76534	08550867-4327596	133.7862435	−43.4666156	885.0 ± 23.1
Hen 3-365	HD 87643	10043028-5839521	151.1265	−58.6645278	1589.1 ± 309.7
HR 5999	HD 144668	16083427-3906181	242.142875	−39.1050278	158.6 ± 0.9
HT Lup	⋯	15451286-3417305	236.3036208	−34.2918389	153.5 ± 1.3
MWC 147	HD 259431	06330519+1019199	98.2716174	10.3222059	653.4 ± 11.6
MWC 166	HD 53367	07042551-1027156	106.1063792	−10.4543722	1219.6 ± 314.4
MWC 275	HD163296	17562128-2157218	269.0886685	−21.9562308	101.0 ± 0.4
MWC 297	⋯	18273952-0349520	276.9146958	−3.831125	417.8 ± 5.3
MWC 614	HD 179218	19111124+1547155	287.7969193	15.7875669	260.1 ± 2.2
MWC 789	HD 250550	06015998+1630567	90.4999527	16.5157295	760.3 ± 28.5
MWC 863	HD150193	16401792-2353452	250.0746503	−23.8959517	150.8 ± 0.5
PDS 66	⋯	13220753-6938121	200.5314458	−69.6367194	97.9 ± 0.1
Ty CrA	⋯	19014081-3652337	285.4201238	−36.8762242	159.1 ± 4.4
V1295 Aql	HD 190073	20030250+0544166	300.7604637	5.7379176	847.9 ± 22.5
V921 Sco	⋯	16590677-4242083	254.7782539	−42.7023413	1482.4 ± 77.4
WRAY 15-535	⋯	10152198-5751427	153.841516	−57.8618381	4989.9 ± 478.1

Note. Distances from Gaia DR3 early release Gaia Collaboration et al. (2021).

Table 2
Gemini-LIGHTS Target Characteristics

Target	Mass ($M_\odot$)	Age (Myr)	Teff (K)	$\log_{10}(L)$ $\log_{10}((L_\odot))$	Disk Classification
AK Sco	$1.4^{+0.07}_{-0.07}$ (b)	$8.38^{+1.72}_{-0.42}$ (b)	6250^{+250}_{-250} (b)	$0.62^{+0.03}_{-0.01}$ (b)	Cont
CU Cha	$2.25^{+0.11}_{-0.14}$ (b)	$4.37^{+1.11}_{-0.32}$ (b)	10500^{+500}_{-500} (b)	$1.54^{+0.07}_{-0.06}$ (b)	Ring
FU Ori	0.3 (f)	2.0 (i)	⋯	⋯	Irr
GW Ori	2.8 (ab)	5.0 (j)	5500.0 (ag)	$1.68^{+0.1}_{-0.08}$ (ah)	Irr
HD 100453	$1.25^{+0.06}_{-0.06}$ (b)	$6.53^{+0.45}_{-0.49}$ (b)	7250^{+250}_{-250} (b)	$0.79^{+0.02}_{-0.0}$ (b)	Spiral, Cont
HD 100546	$2.06^{+0.1}_{-0.12}$ (b)	$5.48^{+1.41}_{-0.77}$ (b)	9750^{+500}_{-500} (b)	$1.37^{+0.07}_{-0.05}$ (b)	Cont
HD 101412	$2.1^{+0.11}_{-0.11}$ (b)	$4.37^{+0.22}_{-0.32}$ (b)	9750^{+250}_{-250} (b)	$1.58^{+0.05}_{-0.04}$ (b)	Nondet
HD 104237	$1.85^{+0.09}_{-0.09}$ (b)	$5.48^{+0.27}_{-0.4}$ (b)	8000^{+250}_{-250} (b)	$1.33^{+0.04}_{-0.01}$ (b)	Undet

Table 2
(Continued)

Target	Mass ($M_\odot$)	Age (Myr)	Teff (K)	$\log_{10}$(L) $\log_{10}$(($L_\odot$))	Disk Classification
HD 139614	$1.48^{+0.07}_{-0.07}$ (b)	$14.49^{+1.41}_{-3.6}$ (b)	7750^{+250}_{-250} (b)	$0.77^{+0.03}_{-0.01}$ (b)	Cont
HD 141569	$1.86^{+0.09}_{-0.09}$ (b)	$8.62^{+11.38}_{-1.19}$ (b)	9750^{+250}_{-250} (b)	$1.22^{+0.03}_{-0.03}$ (b)	Ring
HD 142527	$1.61^{+0.12}_{-0.08}$ (b)	$6.63^{+0.33}_{-1.55}$ (b)	6500^{+250}_{-250} (b)	$0.96^{+0.03}_{-0.0}$ (b)	Spiral, Ring
HD 142666	$1.49^{+0.08}_{-0.08}$ (b)	$9.33^{+0.77}_{-0.47}$ (b)	7500^{+250}_{-250} (b)	$0.94^{+0.04}_{-0.05}$ (b)	Cont
HD 144432	$1.39^{+0.07}_{-0.07}$ (b)	$4.98^{+0.25}_{-0.55}$ (b)	7500^{+250}_{-250} (b)	$0.97^{+0.04}_{-0.01}$ (b)	Nondet
HD 145718	$1.6^{+0.08}_{-0.08}$ (b)	$9.8^{+2.8}_{-0.49}$ (b)	8000^{+250}_{-250} (b)	$0.9^{+0.05}_{-0.04}$ (b)	Cont
HD 158643	$3.35^{+0.79}_{-0.22}$ (b)	$1.22^{+0.29}_{-0.57}$ (b)	9800^{+900}_{-300} (b)	$2.22^{+0.26}_{-0.07}$ (b)	Nondet
HD 169142	$2.0^{+0.13}_{-0.13}$ (b)	$8.98^{+11.02}_{-3.9}$ (b)	10700^{+800}_{-900} (b)	$1.31^{+0.12}_{-0.22}$ (b)	Ring
HD 176386	$2.3^{+0.14}_{-0.3}$ (b)	$4.05^{+15.95}_{-0.57}$ (b)	10700^{+800}_{-900} (b)	$1.58^{+0.12}_{-0.22}$ (b)	Nondet
HD 34700 A	$2.66^{+0.32}_{-0.13}$ (b)	$1.4^{+0.23}_{-0.44}$ (b)	5900^{+110}_{-100} (b)	$1.36^{+0.1}_{-0.02}$ (b)	Spiral, Ring
HD 36917	$3.71^{+0.94}_{-0.75}$ (b)	$0.99^{+0.9}_{-0.5}$ (b)	11215^{+1109}_{-1316} (b)	$2.43^{+0.24}_{-0.29}$ (b)	Nondet
HD 37806	$3.11^{+0.55}_{-0.33}$ (b)	$1.56^{+0.64}_{-0.6}$ (b)	10475^{+1025}_{-675} (b)	$2.17^{+0.19}_{-0.14}$ (b)	Undet
HD 38087	$3.21^{+0.79}_{-0.38}$ (b)	$1.75^{+9.15}_{-0.64}$ (b)	13600^{+2900}_{-830} (b)	$2.19^{+0.3}_{-0.22}$ (b)	Nondet
HD 45677	$4.72^{+1.19}_{-0.39}$ (b)	$0.61^{+3.77}_{-0.3}$ (b)	16500^{+3000}_{-750} (b)	$2.88^{+0.32}_{-0.17}$ (b)	Cont
HD 50138	$4.17^{+0.46}_{-0.33}$ (b)	$0.63^{+0.19}_{-0.18}$ (b)	9450^{+450}_{-450} (b)	$2.46^{+0.13}_{-0.09}$ (b)	Cont
HD 85567	$6.32^{+0.53}_{-0.39}$ (b)	$0.22^{+0.05}_{-0.05}$ (b)	13000^{+500}_{-500} (b)	$3.19^{+0.1}_{-0.08}$ (b)	Undet
HD 95881	$5.5^{+0.5}_{-0.28}$ (b)	$0.28^{+0.05}_{-0.07}$ (b)	10000^{+250}_{-250} (b)	$2.85^{+0.1}_{-0.07}$ (b)	Undet
HD 98800	0.7 (ab)	$8.5^{+1.5}_{-1.5}$ (h)	4200 (al)	0.33 (al)	Undet
HD 98922	$6.17^{+0.37}_{-0.31}$ (b)	$0.2^{+0.01}_{-0.04}$ (b)	10500^{+250}_{-250} (b)	$3.03^{+0.06}_{-0.05}$ (b)	Undet
Hen 3-1330	9.0	…	22280 (ai)	5.3 (ai)	Nondet
Hen 3-225	$7.46^{+0.51}_{-0.37}$ (b)	$0.17^{+0.02}_{-0.03}$ (b)	19000^{+500}_{-500} (b)	$3.55^{+0.09}_{-0.07}$ (b)	Nondet
Hen 3-365	$17.72^{+10.87}_{-6.72}$ (b)	$0.02^{+0.05}_{-0.01}$ (b)	19500^{+5000}_{-3000} (b)	$4.6^{+0.64}_{-0.53}$ (b)	Irr
HR 5999	$2.43^{+0.12}_{-0.12}$ (b)	$2.73^{+0.26}_{-0.35}$ (b)	8500^{+250}_{-250} (b)	$1.72^{+0.05}_{-0.04}$ (b)	Nondet
HT Lup	$1.3^{+0.2}_{-0.2}$ (d)	$0.5^{+0.02}_{-0.4}$ (d)	4247^{+161}_{-237} (k)	$0.51^{+0.01}_{-0.01}$ (k)	Ring
MWC 147	$5.16^{+1.84}_{-1.29}$ (b)	$0.42^{+0.53}_{-0.28}$ (b)	14000^{+2125}_{-2900} (b)	$2.97^{+0.27}_{-0.4}$ (b)	Nondet
MWC 166	$12.3^{+4.2}_{-4.2}$ (e)	$0.08^{+0.08}_{-0.08}$ (e)	29500^{+1000}_{-1000} (e)	$4.11^{+0.37}_{-0.37}$ (e)	Nondet
MWC 275	$1.83^{+0.09}_{-0.09}$ (b)	$7.6^{+1.05}_{-1.22}$ (b)	9250^{+250}_{-250} (b)	$1.2^{+0.06}_{-0.03}$ (b)	Ring
MWC 297	$16.9^{+1.87}_{-1.22}$ (b)	$0.03^{+0.01}_{-0.01}$ (b)	24500^{+1500}_{-1500} (b)	$4.59^{+0.12}_{-0.12}$ (b)	Cont
MWC 614	$2.98^{+0.18}_{-0.3}$ (b)	$1.66^{+0.54}_{-0.26}$ (b)	9500^{+200}_{-200} (b)	$2.05^{+0.09}_{-0.14}$ (b)	Cont
MWC 789	$2.6^{+0.3}_{-0.14}$ (b)	$2.56^{+0.43}_{-0.67}$ (b)	11000^{+500}_{-500} (b)	$1.94^{+0.17}_{-0.12}$ (b)	Irr
MWC 863	$1.89^{+0.1}_{-0.1}$ (b)	$5.48^{+0.44}_{-0.27}$ (b)	9000^{+250}_{-250} (b)	$1.37^{+0.04}_{-0.04}$ (b)	Undet
PDS 66	1.2 (ak)	$6.0^{+1.0}_{-1.0}$ (g)	5035^{+19}_{-19} (ak)	$0.0^{+0.01}_{-0.01}$ (ak)	Ring
Ty CrA	$2.06^{+0.22}_{-0.19}$ (b)	$6.38^{+13.62}_{-2.01}$ (b)	10700^{+800}_{-900} (b)	$1.41^{+0.14}_{-0.23}$ (b)	Nondet
V1295 Aql	$5.89^{+0.8}_{-0.76}$ (b)	$0.22^{+0.11}_{-0.07}$ (b)	9500^{+200}_{-200} (b)	$2.9^{+0.16}_{-0.2}$ (b)	Nondet
V921 Sco	$19.96^{+6.98}_{-5.0}$ (b)	$0.02^{+0.03}_{-0.01}$ (b)	29000^{+3882}_{-4500} (b)	$4.76^{+0.33}_{-0.34}$ (b)	Undet
WRAY 15-535	$17.5^{+2.5}_{-2.5}$ (c)	…	20000^{+3000}_{-3000} (aj)	6.0 (aj)	Undet

Note. Stellar and disk characteristics of stellar mass, Age, Teff, Luminosity, and our disk classification. Disk classification described in Section 4.2. In the table Undet is short for Undetermined and Nondet is short for Nondetections. Citations for specific values are from the following: (b) Vioque et al. (2018), (c) Maravelias et al. (2018), (d) Garufi et al. (2020), (e) Fairlamb et al. (2015), (f) Zhu et al. (2007), (g) Murphy et al. (2013), (h) Ribas et al. (2018), (i) Beck & Aspin (2012), (j) Monnier et al. (2019), (k) Gaia Collaboration et al. (2018), (l) Takami et al. (2018).

Table 3
Gemini-LIGHTS Photometry and Meeus Group

Target	WISE 2 (mag)	WISE 4 (mag)	*J* band (mag)	*H* band (mag)	Meeus Group
AK Sco	4.8 ± 0.036	0.888 ± 0.023	7.676 ± 0.026	7.059 ± 0.033	II
CU Cha	4.3 ± 0.043	−1.309 ± 0.013	7.267 ± 0.023	6.665 ± 0.049	I
FU Ori	3.509 ± 0.065	0.175 ± 0.021	6.519 ± 0.023	5.699 ± 0.033	…
GW Ori	4.208 ± 0.045	−0.74 ± 0.011	7.698 ± 0.03	7.103 ± 0.029	I
HD 100453	3.388 ± 0.065	−1.355 ± 0.007	6.945 ± 0.026	6.39 ± 0.038	I
HD 100546	3.156 ± 0.049	−3.565 ± 0.001	6.425 ± 0.02	5.962 ± 0.031	I
HD 101412	4.94 ± 0.031	1.325 ± 0.013	8.635 ± 0.023	8.217 ± 0.047	II
HD 104237	2.469 ± 0.071	−0.909 ± 0.009	5.813 ± 0.023	5.246 ± 0.059	II
HD 139614	5.099 ± 0.03	−0.667 ± 0.008	7.669 ± 0.026	7.333 ± 0.04	I
HD 141569	6.469 ± 0.02	1.847 ± 0.012	6.872 ± 0.027	6.861 ± 0.04	I

Table 3
(Continued)

Target	WISE 2 (mag)	WISE 4 (mag)	*J* band (mag)	*H* band (mag)	Meeus Group
HD 142527	3.066 ± 0.076	−0.794 ± 0.009	6.503 ± 0.029	5.715 ± 0.031	II
HD 142666	4.145 ± 0.049	−0.065 ± 0.023	7.351 ± 0.026	6.739 ± 0.027	II
HD 144432	4.398 ± 0.044	0.042 ± 0.016	7.095 ± 0.032	6.538 ± 0.067	II
HD 145718	4.848 ± 0.04	0.585 ± 0.015	7.69 ± 0.024	7.263 ± 0.029	II
HD 158643	2.171 ± 0.091	−0.028 ± 0.014	4.9 ± 0.186	4.712 ± 0.206	II
HD 169142	5.593 ± 0.023	−0.561 ± 0.008	7.31 ± 0.021	6.911 ± 0.038	I
HD 176386	6.074 ± 0.015	−0.455 ± 0.012	6.847 ± 0.02	6.809 ± 0.031	I
HD 34700 A	6.794 ± 0.016	0.993 ± 0.008	8.041 ± 0.023	7.706 ± 0.023	I
HD 36917	4.278 ± 0.044	1.153 ± 0.025	7.221 ± 0.019	6.964 ± 0.034	II
HD 37806	3.419 ± 0.115	0.116 ± 0.051	7.115 ± 0.02	6.252 ± 0.033	II
HD 38087	7.207 ± 0.018	1.889 ± 0.019	7.588 ± 0.024	7.386 ± 0.042	I
HD 45677	1.812 ± 0.03	−2.895 ± 0.001	7.242 ± 0.026	6.347 ± 0.023	I
HD 50138	1.585 ± 0.08	−2.078 ± 0.001	5.856 ± 0.027	5.093 ± 0.029	II
HD 85567	3.291 ± 0.062	0.454 ± 0.016	7.472 ± 0.024	6.68 ± 0.031	II
HD 95881	3.125 ± 0.069	0.513 ± 0.008	7.384 ± 0.026	6.662 ± 0.044	II
HD 98800	5.325 ± 0.032	0.194 ± 0.01	6.397 ± 0.02	5.759 ± 0.027	…
HD 98922	1.863 ± 0.014	−1.054 ± 0.006	6.004 ± 0.02	5.226 ± 0.029	II
Hen 3-1330	3.344 ± 0.063	1.95 ± 0.02	6.713 ± 0.024	6.103 ± 0.042	…
Hen 3-225	7.066 ± 0.02	4.193 ± 0.027	7.818 ± 0.024	7.858 ± 0.04	II
Hen 3-365	2.248 ± 0.018	−3.988 ± 0.001	6.217 ± 0.037	4.756 ± 0.268	…
HR 5999	1.895 ± 0.012	−0.541 ± 0.01	5.907 ± 0.018	5.22 ± 0.027	II
HT Lup	4.973 ± 0.032	0.856 ± 0.016	7.573 ± 0.021	6.866 ± 0.029	…
MWC 147	3.169 ± 0.074	−0.757 ± 0.013	7.454 ± 0.026	6.666 ± 0.034	II
MWC 166	4.538 ± 0.044	1.051 ± 0.059	6.332 ± 0.02	6.22 ± 0.033	…
MWC 275	2.466 ± 0.061	−0.758 ± 0.007	6.195 ± 0.021	5.531 ± 0.036	II
MWC 297	1.872 ± 0.018	−4.718 ± 0.001	6.127 ± 0.019	4.387 ± 0.214	…
MWC 614	3.647 ± 0.051	−1.606 ± 0.006	6.994 ± 0.02	6.645 ± 0.026	I
MWC 789	4.633 ± 0.039	0.046 ± 0.015	8.475 ± 0.02	7.528 ± 0.026	II
MWC 863	3.244 ± 0.065	−0.592 ± 0.012	6.947 ± 0.02	6.214 ± 0.02	II
PDS 66	6.183 ± 0.022	1.587 ± 0.016	8.277 ± 0.032	7.641 ± 0.023	…
Ty CrA	5.139 ± 0.027	−2.35 ± 0.011	7.486 ± 0.024	6.97 ± 0.026	I
V1295 Aql	3.443 ± 0.064	0.589 ± 0.016	7.194 ± 0.019	6.647 ± 0.017	II
V921 Sco	2.045 ± 0.02	−4.143 ± 0.001	7.235 ± 0.027	5.918 ± 0.045	…
WRAY 15-535	1.556 ± 0.011	−0.231 ± 0.011	5.762 ± 0.018	4.959 ± 0.059	…

Note. WISE photometry from the WISE All-sky survey (Cutri et al. 2012) and *J*- and *H*-band photometry from the 2MASS survey (Cutri et al. 2003). The Meeus Group is categorized in this work as described in Section 5. Notes: (a) Lieman-Sifry et al. (2016), (b) Henning et al. (1993), (c) Liu et al. (2018), (d) Fang et al. (2017), (e) this work, (f) Sylvester et al. (1996), (g) van der Plas et al. (2019), (h) Miley et al. (2019), (i) Nilsson et al. (2010), (j) Kataoka et al. (2016), (k) Ansdell et al. (2018), (l) Andrews et al. (2018), (m) Cazzoletti et al. (2019), (n) Benac et al. (2020).

Table 4
Observational Log and Stellar/Instrumental Polarization

Target	Filter	Epoch (YYYYMMDD)	Exposure Time (s)	# of Frames	Stellar/Instrumental Polarization	
					% Pol	PA (°)
AK Sco	H	20180811	59.6	40	1.69 ± 0.06	138 ± 1
CU Cha	J	20170406	58.2	32	1.42 ± 0.12	117 ± 3
CU Cha	H	20180413	58.2	36	1.5 ± 0.12	112 ± 2
FU Ori	J	20180103	58.2	24	0.16 ± 0.03	87 ± 6
GW Ori	J	20180104	58.2	32	0.48 ± 0.1	96 ± 6
GW Ori	H	20180104	58.2	36	0.34 ± 0.11	110 ± 10
HD 100453	J	20150410	14.5	140	0.07 ± 0.22	41 ± 93
HD 100546	J	20170220	43.6	40	1.16 ± 0.07	60 ± 2
HD 101412	H	20180319	59.6	40	0.68 ± 0.05	92 ± 2
HD 104237	J	20170407	58.2	32	0.44 ± 0.05	98 ± 3
HD 104237	J	20180317	58.2	32	0.31 ± 0.01	94 ± 1
HD 104237	J	20180520	58.2	32	0.38 ± 0.04	119 ± 3
HD 104237	J	20190217	58.2	32	0.51 ± 0.04	121 ± 2
HD 139614	J	20170406	58.2	64	0.46 ± 0.09	179 ± 5

Table 4
(Continued)

Target	Filter	Epoch (YYYYMMDD)	Exposure Time (s)	# of Frames	Stellar/Instrumental Polarization	
					% Pol	PA (°)
HD 139614	H	20180608	58.2	28	0.56 ± 0.03	11 ± 1
HD 139614	J	20190513	58.2	36	0.17 ± 0.08	130 ± 14
HD 141569	J	20180609	58.2	32	0.65 ± 0.05	105 ± 2
HD 141569	J	20190223	58.2	32	0.52 ± 0.06	114 ± 3
HD 142527	H	20140425	4.4	92	0.81 ± 0.15	40 ± 5
HD 142666	J	20170703	58.2	20	0.49 ± 0.06	84 ± 4
HD 142666	J	20180609	58.2	32	0.46 ± 0.02	79 ± 1
HD 144432	H	20150709	58.2	32	1.26 ± 0.09	175 ± 2
HD 145718	J	20180607	58.2	32	1.08 ± 0.16	102 ± 4
HD 145718	H	20180608	58.2	32	1.51 ± 0.18	82 ± 3
HD 158643	J	20180609	58.2	32	0.5 ± 0.06	1 ± 3
HD 158643	J	20190223	58.2	32	0.55 ± 0.02	3 ± 1
HD 169142	J	20140425	58.2	56	0.45 ± 0.13	175 ± 8
HD 176386	H	20180607	58.2	32	0.28 ± 0.02	2 ± 2
HD 176386	H	20180816	58.2	32	0.27 ± 0.05	2 ± 5
HD 176386	J	20180817	58.2	64	0.15 ± 0.14	40 ± 27
HD 34700 A	J	20180103	58.2	32	0.65 ± 0.13	102 ± 6
HD 34700 A	H	20180103	58.2	32	0.36 ± 0.05	104 ± 4
HD 36917	J	20171231	58.2	32	0.21 ± 0.03	31 ± 4
HD 36917	H	20190126	58.2	36	0.79 ± 0.03	44 ± 1
HD 37806	J	20171231	58.2	32	0.89 ± 0.05	129 ± 2
HD 38087	J	20180103	58.2	32	1.3 ± 0.06	109 ± 1
HD 45677	J	20171231	58.2	32	0.42 ± 0.04	46 ± 3
HD 45677	H	20180101	58.2	32	0.46 ± 0.04	11 ± 3
HD 50138	J	20180104	58.2	32	0.29 ± 0.06	143 ± 6
HD 85567	J	20180103	58.2	32	0.45 ± 0.05	71 ± 3
HD 85567	J	20180520	58.2	32	0.46 ± 0.02	128 ± 1
HD 85567	H	20190127	58.2	28	0.48 ± 0.03	84 ± 2
HD 95881	J	20180104	58.2	40	0.91 ± 0.09	86 ± 3
HD 98800	H	20190127	34.9	28	0.74 ± 0.1	154 ± 4
HD 98922	J	20180321	58.2	32	0.41 ± 0.07	64 ± 5
Hen 3-1330	J	20190512	58.2	32	2.02 ± 0.06	27 ± 1
Hen 3-225	J	20190127	58.2	32	0.47 ± 0.05	147 ± 3
Hen 3-225	H	20190127	58.2	32	0.21 ± 0.08	39 ± 12
Hen 3-365	J	20170406	58.2	32	0.79 ± 0.09	166 ± 3
HR 5999	J	20170406	58.2	32	1.13 ± 0.11	28 ± 3
HR 5999	J	20170702	58.2	36	0.32 ± 0.19	19 ± 17
HT Lup	H	20190514	52.4	64	0.77 ± 0.12	36 ± 4
MWC 147	J	20171231	58.2	32	0.79 ± 0.02	88 ± 1
MWC 147	H	20190127	58.2	32	1.0 ± 0.07	97 ± 2
MWC 166	J	20170406	58.2	16	0.81 ± 0.05	48 ± 2
MWC 275	J	20140424	58.2	32	0.8 ± 0.34	34 ± 12
MWC 297	H	20180608	58.2	32	1.21 ± 0.05	94 ± 1
MWC 297	H	20180817	43.6	32	1.15 ± 0.04	99 ± 1
MWC 614	J	20180816	58.2	64	0.94 ± 0.07	95 ± 2
MWC 614	H	20180816	58.2	64	1.24 ± 0.11	101 ± 2
MWC 789	H	20181120	58.2	40	0.92 ± 0.13	37 ± 4
MWC 863	J	20140424	58.2	32	2.95 ± 0.28	56 ± 3
PDS 66	J	20160306	59.6	104	0.82 ± 0.06	99 ± 2
Ty CrA	H	20180608	58.2	32	0.33 ± 0.04	148 ± 3
Ty CrA	H	20180817	52.4	32	0.15 ± 0.04	164 ± 7
V1295 Aql	H	20180608	58.2	32	0.59 ± 0.06	104 ± 3
V1295 Aql	J	20180816	58.2	64	0.58 ± 0.06	75 ± 3
V1295 Aql	H	20180816	58.2	32	0.56 ± 0.04	53 ± 2
V921 Sco	H	20190513	58.2	32	0.98 ± 0.21	138 ± 6
WRAY 15-535	J	20180319	58.2	32	2.1 ± 0.09	53 ± 1
WRAY 15-535	J	20190222	58.2	32	2.02 ± 0.1	58 ± 1

Note. All epochs observed as part of the Gemini-LIGHTS survey. PA and %Pol are the average polarization angle and % polarization of stellar and instrumental polarization removed.

Table 5
Polarization Flux and Point-source Detection Upper Limits

Target	Band	Epoch (YYYYMMDD)	Q_ϕ /Fstar (per 1000)	5σ Point-source Detection Upper limit	
				Contrast at $0\farcs2$	Mass Sensitivity ($M_\odot$)
AK Sco	H	20180811	1.2 ± 0.2	1.6E-04	0.011
CU Cha	J	20170406	2.7 ± 0.9	3.9E-05	0.006
CU Cha	H	20180413	3.8 ± 1.0	2.5E-04	0.02
FU Ori	J	20180103	3.7 ± 0.6	1.2E-04	0.03
GW Ori	J	20180104	9.4 ± 0.9	1.6E-04	0.011
GW Ori	H	20180104	13.3 ± 1.1	5.9E-05	0.007
HD 34700 A	J	20180103	15.7 ± 1.8	1.3E-04	0.008
HD 34700 A	H	20180103	22.2 ± 1.8	5.3E-05	0.005
HD 36917	J	20171231	<0.02	3.6E-05	0.007
HD 36917	H	20190126	<0.03	8.6E-05	0.01
HD 37806	J	20171231	<0.04	3.8E-05	0.008
HD 38087	J	20180103	<0.12	6.1E-05	0.008
HD 45677	J	20171231	8.4 ± 1.1	5.5E-05	0.01
HD 45677	H	20180101	6.9 ± 1.0	3.0E-05	0.01
HD 50138	J	20180104	0.9 ± 0.2	6.0E-05	0.011
HD 85567	J	20180103	0.10 ± 0.08	1.0E-04	0.03
HD 85567	J	20180520	0.12 ± 0.07	4.7E-05	0.02
HD 85567	H	20190127	0.13 ± 0.11	2.5E-04	0.06
HD 95881	J	20180104	<0.09	9.6E-05	0.03
HD 98800	H	20190127	0.19 ± 0.14	⋯	⋯
HD 98922	J	20180321	0.21 ± 0.16	6.9E-05	0.03
HD 100453	J	20150410	2.9 ± 0.2	⋯	⋯
HD 100546	J	20170220	10.2 ± 0.6	8.7E-05	0.008
HD 101412	H	20180319	<0.04	1.7E-04	0.013
HD 104237	J	20170407	0.04 ± 0.03	9.2E-05	0.013
HD 104237	J	20180317	0.03 ± 0.02	1.6E-04	0.014
HD 104237	J	20180520	0.06 ± 0.03	2.2E-04	0.02
HD 104237	J	20190217	<0.06	1.4E-04	0.014
HD 139614	J	20170406	2.5 ± 0.7	8.9E-05	0.01
HD 139614	J	20190513	1.5 ± 0.6	6.7E-05	0.009
HD 139614	H	20180608	2.5 ± 0.7	3.1E-03	0.06
HD 141569	J	20180609	0.29 ± 0.28	1.5E-04	0.013
HD 141569	J	20190223	<0.3	4.8E-05	0.007
HD 142527	H	20140425	9.26 ± 1.17	⋯	⋯
HD 142666	J	20170703	0.19 ± 0.17	⋯	⋯
HD 142666	J	20180609	0.09 ± 0.08	⋯	⋯
HD 144432	H	20150709	<0.03	⋯	⋯
HD 145718	J	20180607	0.4 ± 0.3	4.4E-05	0.007
HD 145718	H	20180608	0.4 ± 0.2	1.1E-04	0.011
HD 158643	J	20180609	<0.01	2.4E-05	0.005
HD 158643	J	20190223	<0.04	⋯	⋯
HD 169142	J	20140425	4.5 ± 0.8	1.0E-04	0.008
HD 176386	J	20180817	<0.01	2.8E-05	0.005
HD 176386	H	20180607	<0.05	6.7E-05	0.006
HD 176386	H	20180816	<0.02	6.8E-05	0.006
Hen 3-1330	J	20190512	<0.03	4.8E-05	0.04
Hen 3-225	J	20190127	<0.04	7.3E-05	0.013
Hen 3-225	H	20190127	<0.06	6.7E-05	0.01
Hen 3-365	J	20170406	5.5 ± 0.6	3.3E-05	0.05
HR 5999	J	20170406	<0.02	3.3E-04	0.03
HR 5999	J	20170702	0.03 ± 0.02	7.8E-05	0.01
HT Lup	H	20190514	0.4 ± 0.2	5.6E-04	0.009
MWC 147	J	20171231	<0.07	8.4E-05	0.011
MWC 147	H	20190127	<0.1	3.3E-04	0.04
MWC 166	J	20170406	<0.06	6.0E-03	1.4
MWC 275	J	20140424	0.3 ± 0.2	7.3E-05	0.01
MWC 297	H	20180608	0.3 ± 0.2	8.5E-05	0.04
MWC 297	H	20180817	0.3 ± 0.2	1.0E-04	0.04
MWC 614	J	20180816	2.0 ± 0.3	1.5E-04	0.014
MWC 614	H	20180816	2.4 ± 0.2	1.7E-04	0.013
MWC 789	H	20181120	5.9 ± 1.5	6.3E-04	0.06
MWC 863	J	20140424	<0.3	1.1E-03	0.03
PDS 66	J	20160306	2.2 ± 1.1	5.9E-05	0.003

Table 5
(Continued)

Target	Band	Epoch (YYYYMMDD)	Q_ϕ /Fstar (per 1000)	5σ Point-source Detection Upper limit	
				Contrast at 0″2	Mass Sensitivity ($M_\odot$)
Ty CrA	H	20180608	<0.6	8.7E-04	0.3
Ty CrA	H	20180817	<0.44	1.5E-04	0.06
V1295 Aql	J	20180816	<0.02	2.5E-04	0.05
V1295 Aql	H	20180608	<0.02	1.0E-04	0.03
V1295 Aql	H	20180816	<0.04	2.9E-04	0.05
V921 Sco	H	20190513	0.06 ± 0.05	1.6E-04	0.13
WRAY 15-535	J	20180319	0.11 ± 0.07	1.0E-04	⋯
WRAY 15-535	J	20190222	<0.04	1.5E-05	⋯

Note. Mass estimate based on measured companion flux and the system age (see Table 2 and use models from Baraffe et al. (2015) for masses >0.01 $M_\odot$ and Phillips et al. (2020) for masses <0.01 $M_\odot$. The Q_ϕ /Fstar values utilized in this work are the weighted average of the epochs listed above.

Table 6
Point Sources Detected in the Gemini-LIGHTS Sample

Target	Band	Epoch (YYYYMMDD)	Comp. #	Separation (″)	PA (°)	Flux (mJy)	Saturated	Mass Est. ($M_\odot$)
FU Ori	J	20180103	1	0.431 ± 0.003	163.3 ± 0.3	27 ± 4	TRUE	$0.6^{+0.1}_{-0.1}$
HD 100453	J	20150411	1	0.909 ± 0.002	131.63 ± 0.09	15.4 ± 1.3	FALSE	$0.08^{+0.01}_{-0.04}$
HD 101412	H	20180319	1	0.460 ± 0.002	149.9 ± 0.2	1.46 ± 0.11	FALSE	$0.053^{+0.03}_{-0.003}$
HD 101412	H	20180319	2	0.153 ± 0.003	184.9 ± 1.0	5.0 ± 0.4	FALSE	$0.19^{+0.06}_{-0.01}$
HD 104237	J	20170407	1	1.226 ± 0.004	255.43 ± 0.14	29 ± 9	FALSE	$0.11^{+0.04}_{-0.04}$
HD 104237	J	20180317	1	1.214 ± 0.004	255.034 ± 0.13	19 ± 6	FALSE	$0.065^{+0.02}_{-0.02}$
HD 104237	J	20180520	1	1.204 ± 0.003	255.1 ± 0.11	32 ± 6	FALSE	$0.12^{+0.02}_{-0.02}$
HD 104237	J	20190217	1	1.198 ± 0.004	255.28 ± 0.11	34 ± 5	FALSE	$0.13^{+0.02}_{-0.02}$
HD 144432	H	20150708	1	1.256 ± 0.004	6.07 ± 0.16	51 ± 7	TRUE	$0.3^{+0.03}_{-0.05}$
HD 158643	J	20180609	1	0.118 ± 0.013	294 ± 5	30 ± 4	FALSE	$0.07^{+0.01}_{-0.02}$
HD 38087	J	20180103	1	0.303 ± 0.003	183.7 ± 0.4	47 ± 8	TRUE	$0.8^{+0.5}_{-0.3}$
HD 50138	J	20180104	1	0.729 ± 0.003	106.6 ± 0.2	10.1 ± 1.5	FALSE	$^{*}0.12$
HD 98800	H	20190127	1	0.374 ± 0.010	9.8 ± 0.6	633 ± 9	TRUE	$0.4^{+0.03}_{-0.03}$
HR 5999	J	20170406	1	1.251 ± 0.004	112.55 ± 0.11	141 ± 16	TRUE	$0.6^{+0.1}_{-0.2}$
HR 5999	J	20170702	1	1.260 ± 0.005	112.4 ± 0.2	128 ± 19	TRUE	$0.6^{+0.1}_{-0.2}$
HT Lup	H	20190514	1	0.161 ± 0.003	246.6 ± 0.7	70 ± 7	TRUE	$0.13^{+0.01}_{-0.01}$
Hen 3-365	J	20170406	1	0.818 ± 0.003	101.08 ± 0.14	1.3 ± 0.2	FALSE	$^{*}0.17$
Hen 3-365	J	20170406	2	0.446 ± 0.008	133.0 ± 0.8	0.6 ± 0.1	FALSE	$^{*}0.13$
Hen 3-225	J	20190127	1	1.564 ± 0.019	303.4 ± 0.3	1.46 ± 0.02	FALSE	$^{*}0.12$
Hen 3-1330	J	20190512	1	0.268 ± 0.017	49 ± 2	0.8 ± 0.3	FALSE	$^{*}0.13$
MWC 147	J	20171231	1	0.137 ± 0.004	56 ± 1	30 ± 6	TRUE	$0.6^{+0.4}_{-0.1}$
MWC 147	J	20190127	1	0.156 ± 0.003	54.1 ± 0.8	33 ± 5	TRUE	$0.5^{+0.4}_{-0.1}$
MWC 166	J	20170406	1	0.587 ± 0.004	298.4 ± 0.3	282 ± 9	TRUE	$^{*} > 1.4$
MWC 297	H	20180608	1	0.573 ± 0.003	86.5 ± 0.2	2.06 ± 0.09	FALSE	$^{*}0.04$
MWC 297	H	20180817	1	0.576 ± 0.004	86.6 ± 0.2	1.74 ± 0.14	FALSE	$^{*}0.04$
MWC 789	H	20181120	1	0.371 ± 0.002	216.8 ± 0.3	10.7 ± 0.8	FALSE	$0.8^{+0.1}_{-0.2}$
MWC 863	J	20140421	1	0.975 ± 0.004	226.97 ± 0.14	154 ± 19	TRUE	$0.8^{+0.1}_{-0.1}$
Ty CrA	H	20180608	1	0.129 ± 0.004	255.2 ± 1.3	26 ± 4	FALSE	>1.4
Ty CrA	H	20180817	1	0.112 ± 0.003	257.3 ± 1.0	41 ± 4	FALSE	>1.4
V921 Sco	H	20190513	1	0.475 ± 0.013	319.0 ± 1.1	0.09 ± 0.03	FALSE	$0.03^{+0.01}_{-0.01}$
V921 Sco	H	20190513	2	1.122 ± 0.003	323.12 ± 0.09	0.96 ± 0.08	FALSE	$0.15^{+0.01}_{-0.01}$
V1295 Aql	H	20180608	1	1.113 ± 0.003	40.52 ± 0.11	0.026 ± 0.002	FALSE	$^{*}0.010$
V1295 Aql	H	20180816	1	1.135 ± 0.016	40.1 ± 0.5	0.055 ± 0.009	FALSE	$^{*}0.013$
V1295 Aql	J	20180817	1	1.119 ± 0.005	40.6 ± 0.2	0.015 ± 0.002	FALSE	$^{*}0.010$

Note. Point sources with their PSF cores saturated are noted in the table. Mass estimate based on measured companion flux and the system age (see Table 2). Mass estimates use models from Baraffe et al. (2015) for masses >0.01 $M_\odot$ and Phillips et al. (2020) for masses <0.01 $M_\odot$. A * denotes any target with ages <0.5 Myr that are younger than the youngest model in Baraffe et al. (2015) or Phillips et al. (2020).

Appendix B
Polarized Light FITS header Definition

Here we define a standard FITS file for high-contrast polarization data. This is motivated by large numbers of observations of protoplanetary disks from multiple telescopes (e.g., GPI, SPHERE/IRDIS, Subaru/HiCIAO, Subaru/CHARIS). A standard FITS file will allow for better comparison of protoplanetary disk polarization imagery between different studies and instruments. This FITS standard was created in collaboration with Christian Ginski.

The data are held in a three-dimensional cube of $5 \times x \times y$, where x and y are the pixel dimensions of the image, and 5 are the different image types. The five different image types are I, Q_ϕ , U_ϕ , Q, U, and :LP_I where I is the intensity image without stellar light subtracted, Q_ϕ , U_ϕ , Q, and U as defined above in Section 3, and LP_I, which is the linear polarized intensity or $(Q^2 + U^2)^{1/2}$.

A sample header is shown in Table 7 taken from GPI observations of MWC 275 (HD 163296) used in this work. Standard WCS headers are included to allow use and image overlay with programs such as DS9. Additionally, reduction information such as star locations (X-STAR, Y-STAR), flux

Table 7
Sample Header

Keyword	Value	Comment
DATE-OBS	"2014-04-24"	UT start date of exposure
CCDSIZE	"2048x2048"	Array dimensions
CREATOR	"GPI DRP, v1.5.0,revc0cad3f"	This file created by GPI Data Reduction
OBSMODE	"J_coron"	Currently selected observation mode
RA	269.0887	Target R.A.
DEC	−21.956075	Target decl.
DATE	"2014-04-24"	UTC Date of observation (YYYY-MM-DD)
EPOCH	2000.0	Target Coordinate Epoch
GEMPRGID	"GS-2014A-SV-412"	Gemini program ID
INSTRUME	"GPI"	Instrument used to acquire data
OBSERVAT	"Gemini South"	Observatory (Gemini-North|Gemini South)
OBSID	"GS-2014A-SV-412-6"	Gemini Observation ID
CD1_1	−3.92777777778E-06	partial of first axis coordinate w.r.t. *x*
CD1_2	9.84069992011E-14	partial of first axis coordinate w.r.t. *y*
CD2_1	9.8406999118E-14	partial of second axis coordinate w.r.t. *x*
CD2_2	3.92777777778E-06	partial of second axis coordinate w.r.t. *y*
CDELT1	0.0014	Coordinate increment
CDELT2	0.0014	Coordinate increment
CRPIX1	141.0	*x*-coordinate of ref pixel [note: first pixel is
CRPIX2	141.0	*y*-coordinate of ref pixel [note: first pixel is
CRVAL1	269.0887	R.A. at ref point
CRVAL2	−21.956075	decl. at ref point
CTYPE1	"RA–TAN"	First axis is R.A.
CTYPE2	"DEC–TAN"	Second axis is decl.
CUNIT1	"deg"	Units of data
CUNIT2	"deg"	Units of data
RADESYS	"FK5"	R.A decl. coordinate system reference
BSCALE	1	Linear factor in scaling equation
BZERO	0	Zero-point in scaling equation
WCSAXES	3	Number of axes in WCS system
CTYPE3	"STOKES"	Polarization
CUNIT3	"N/A"	Polarizations
CRVAL3	1	I,Q_phi,U_phi,Q,U,LP_I
CRPIX3	0	Reference pixel location
CD3_3	1	Stokes axis: images 0 and 1 give orthogonal pol
FQ	0.002997042052516556	avg frac of stell/inst pol removed
FU	0.007443801664624007	avg frac of stell/inst pol removed
TARGET	"MWC_275"	Target Name
STOKES	"I,Q_phi,U_phi,Q,U,LP_I"	data cube Stokes components
STAR_X	140.5	star position axis1 (1-based coordinates)
STAR_Y	140.5	star position axis2 (1-based coordinates)
FILTER	"*J*-band "	filter band of observation
ZEROPT	1594	Jy
REFMAG	6.195	ref. mag of star for flux conversion
FLUXUNIT	"mJy/arcseĉ2"	pixel flux units
CALIBFAC	4.00356E-08	Conversion factor mJy/arcseĉ2/ADU/sec/coadd
SCALE	14.14	Pixel Scale mas/pix
COMMENT	…	Stokes components only take linear pol. into account
COMMENT	…	All pol. images are stellar pol. subtracted.
COMMENT	…	2MASS magnitudes used for flux conversion

calibration (ZEROPT, REFMAG, CALIBFFAC), and fraction of stellar/instrumental polarization removed (FQ, FU) will help facilitate better comparisons between different epochs of observations of the same target.

ORCID iDs

Evan A. Rich https://orcid.org/0000-0002-1779-8181
John D. Monnier https://orcid.org/0000-0002-3380-3307
Alicia Aarnio https://orcid.org/0000-0002-1327-9659
Anna S. E. Laws https://orcid.org/0000-0002-2145-0487
Benjamin R. Setterholm https://orcid.org/0000-0001-5980-0246
David J. Wilner https://orcid.org/0000-0003-1526-7587
Nuria Calvet https://orcid.org/0000-0002-3950-5386
Tim Harries https://orcid.org/0000-0001-8228-9503
Chris Miller https://orcid.org/0000-0002-1365-0841
Claire L. Davies https://orcid.org/0000-0001-9764-2357
Fred C. Adams https://orcid.org/0000-0002-8167-1767
Sean M. Andrews https://orcid.org/0000-0003-2253-2270
Jaehan Bae https://orcid.org/0000-0001-7258-770X
Catherine Espaillat https://orcid.org/0000-0001-9227-5949
Alexandra Z. Greenbaum https://orcid.org/0000-0002-7162-8036
Sasha Hinkley https://orcid.org/0000-0001-8074-2562
Stefan Kraus https://orcid.org/0000-0001-6017-8773
Lee Hartmann https://orcid.org/0000-0003-1430-8519
Andrea Isella https://orcid.org/0000-0001-8061-2207
Melissa McClure https://orcid.org/0000-0003-1878-327X
Rebecca Oppenheimer https://orcid.org/0000-0001-7130-7681
Laura M. Pérez https://orcid.org/0000-0002-1199-9564
Zhaohuan Zhu https://orcid.org/0000-0003-3616-6822

References

Andrews, S. M., Huang, J., Pérez, L. M., et al. 2018, ApJL, 869, L41
Ansdell, M., Williams, J. P., Trapman, L., et al. 2018, ApJ, 859, 21
Avenhaus, H., Quanz, S. P., Garufi, A., et al. 2018, ApJ, 863, 44
Baraffe, I., Homeier, D., Allard, F., & Chabrier, G. 2015, A&A, 577, A42
Beck, T. L., & Aspin, C. 2012, AJ, 143, 55
Benac, P., Matrà, L., Wilner, D. J., et al. 2020, ApJ, 905, 120
Bressan, A., Marigo, P., Girardi, L., et al. 2012, MNRAS, 427, 127
Calvet, N., D'Alessio, P., Hartmann, L., et al. 2002, ApJ, 568, 1008
Cazzoletti, P., Manara, C. F., Liu, H. B., et al. 2019, A&A, 626, A11
Chauvin, G., Lagrange, A. M., Beust, H., et al. 2003, A&A, 406, L51
Cutri, R. M., Skrutskie, M. F., van Dyk, S., et al. 2003, yCat, II/246
Cutri, R. M., Wright, E. L., Conrow, T., et al. 2012, yCat, II/311
Davies, C. L., Rich, E. A., Harries, T. J., et al. 2022, MNRAS, 511, 2434
De Rosa, R. J., Esposito, T. M., Gibbs, A., et al. 2020, Proc. SPIE, 11447, 114475A
Debes, J. H., Poteet, C. A., Jang-Condell, H., et al. 2017, ApJ, 835, 205
Domiciano de Souza, A., Driebe, T., Chesneau, O., et al. 2007, A&A, 464, 81
Espaillat, C., Muzerolle, J., Najita, J., et al. 2014, in Protostars and Planets VI, ed. H. Beuther et al. (Tucson, AZ: Univ. of Arizona Press), 497
Fairlamb, J. R., Oudmaijer, R. D., Mendigutía, I., Ilee, J. D., & van den Ancker, M. E. 2015, MNRAS, 453, 976
Fang, M., Sicilia-Aguilar, A., Wilner, D., et al. 2017, A&A, 603, A132
Follette, K. B., Rameau, J., Dong, R., et al. 2017, AJ, 153, 264
Gaia Collaboration, Brown, A. G. A., Vallenari, A., et al. 2018, A&A, 616, A1
Gaia Collaboration, Brown, A. G. A., Vallenari, A., et al. 2021, A&A, 649, A1
Garufi, A., Avenhaus, H., Pérez, S., et al. 2020, A&A, 633, A82
Garufi, A., Benisty, M., Pinilla, P., et al. 2018, A&A, 620, A94
Garufi, A., Meeus, G., Benisty, M., et al. 2017, A&A, 603, A21
Ginski, C., Stolker, T., Pinilla, P., et al. 2016, A&A, 595, A112
Giulia Ubeira Gabellini, M., van den Ancker, M., Fedele, D., Lodato, G., & Manara, C. F. 2019, RNAAS, 3, 61
Guzmán-Díaz, J., Mendigutía, I., Montesinos, B., et al. 2020, A&A, 650, A182
Haffert, S. Y., Bohn, A. J., de Boer, J., et al. 2019, NatAs, 3, 749
Henning, T., Pfau, W., Zinnecker, H., & Prusti, T. 1993, A&A, 276, 129
Kant, I. 1755, Allgemeine Naturgeschichte und Theorie des Himmels (Lausanne: Univ. of Lausanne)
Kataoka, A., Tsukagoshi, T., Momose, M., et al. 2016, ApJL, 831, L12
Kennedy, G. M., Matrà, L., Facchini, S., et al. 2019, NatAs, 3, 230
Keppler, M., Benisty, M., Müller, A., et al. 2018, A&A, 617, A44
Kervella, P., Arenou, F., Mignard, F., & Thévenin, F. 2019, A&A, 623, A72
Kluska, J., Kraus, S., Davies, C. L., et al. 2018, ApJ, 855, 44
Kraus, S., Kreplin, A., Young, A. K., et al. 2020, Sci, 369, 1233
Kreplin, A., Kraus, S., Tambovtseva, L., Grinin, V., & Hone, E. 2020, MNRAS, 492, 566
Kurtovic, N. T., Pérez, L. M., Benisty, M., et al. 2018, ApJL, 869, L44
Labdon, A., Kraus, S., Davies, C. L., et al. 2019, A&A, 627, A36
Lang, D., Hogg, D. W., & Schlegel, D. J. 2016, AJ, 151, 36
Larkin, J. E., Chilcote, J. K., Aliado, T., et al. 2014, Proc. SPIE, 9147, 91471K
Laws, A. S. E., Harries, T. J., Setterholm, B. R., et al. 2020, ApJ, 888, 7
Lieman-Sifry, J., Hughes, A. M., Carpenter, J. M., et al. 2016, ApJ, 828, 25
Liimets, T., Kraus, M., Moiseev, A., et al. 2022, Galax, 10, 41
Liu, H. B., Dunham, M. M., Pascucci, I., et al. 2018, A&A, 612, A54
Long, Z. C., Fernandes, R. B., Sitko, M., et al. 2017, ApJ, 838, 62
Maaskant, K. M., Honda, M., Waters, L. B. F. M., et al. 2013, A&A, 555, A64
Macintosh, B., Graham, J. R., Ingraham, P., et al. 2014, PNAS, 111, 12661
Maire, J., Perrin, M. D., Doyon, R., et al. 2010, Proc. SPIE, 7735, 773531
Manoj, P., Ho, P. T. P., Ohashi, N., et al. 2007, ApJL, 667, L187
Maravelias, G., Kraus, M., Cidale, L. S., et al. 2018, MNRAS, 480, 320
Marston, A. P., & McCollum, B. 2008, A&A, 477, 193
Matsumura, S., & Pudritz, R. E. 2003, ApJ, 598, 645
Meeus, G., Waters, L. B. F. M., Bouwman, J., et al. 2001, A&A, 365, 476
Miley, J. M., Panić, O., Haworth, T. J., et al. 2019, MNRAS, 485, 739
Millar-Blanchaer, M. A., Perrin, M. D., Hung, L.-W., et al. 2016, Proc. SPIE, 9908, 990836
Miroshnichenko, A. S., Manset, N., Kusakin, A. V., et al. 2007, ApJ, 671, 828
Monnier, J. D., Harries, T. J., Aarnio, A., et al. 2017, ApJ, 838, 20
Monnier, J. D., Harries, T. J., Bae, J., et al. 2019, ApJ, 872, 122
Muro-Arena, G. A., Benisty, M., Ginski, C., et al. 2020, A&A, 635, A121
Muro-Arena, G. A., Dominik, C., Waters, L. B. F. M., et al. 2018, A&A, 614, A24
Murphy, S. J., Lawson, W. A., & Bessell, M. S. 2013, MNRAS, 435, 1325
Nilsson, R., Liseau, R., Brandeker, A., et al. 2010, A&A, 518, A40
Oudmaijer, R. D., Proga, D., Drew, J. E., & de Winter, D. 1998, MNRAS, 300, 170
Perrin, M. D., Duchene, G., Millar-Blanchaer, M., et al. 2015, ApJ, 799, 182
Perrin, M. D., Maire, J., Ingraham, P., et al. 2014, Proc. SPIE, 9147, 91473J
Phillips, M. W., Tremblin, P., Baraffe, I., et al. 2020, A&A, 637, A38
Poyneer, L. A., De Rosa, R. J., Macintosh, B., et al. 2014, Proc. SPIE, 9148, 91480K
Ribas, Á, Macías, E., Espaillat, C. C., & Duchêne, G. 2018, ApJ, 865, 77
Rich, E. A., Teague, R., Monnier, J. D., et al. 2021, ApJ, 913, 138
Rich, E. A., Wisniewski, J. P., Currie, T., et al. 2019, ApJ, 875, 38
Richardson, N. D., Gies, D. R., & Williams, S. J. 2011, AJ, 142, 201
Rodigas, T. J., Follette, K. B., Weinberger, A., Close, L., & Hines, D. C. 2014, ApJL, 791, L37
Strom, K. M., Strom, S. E., Edwards, S., Cabrit, S., & Skrutskie, M. F. 1989, AJ, 97, 1451
Sturm, J. A., McClure, M. K., Harsono, D., et al. 2022, A&A, 660, A126
Sylvester, R. J., Skinner, C. J., Barlow, M. J., & Mannings, V. 1996, MNRAS, 279, 915
Tamura, M. 2009, in AIP Conf. Ser. 1158, Exoplanets and Disks: Their Formation and Diversity, ed. T. Usuda, M. Tamura, & M. Ishii (Melville, NY: AIP), 11
Takami, M., Fu, G., Liu, H. B., et al. 2018, ApJ, 864, 20
Ubeira-Gabellini, M. G., Christiaens, V., Lodato, G., et al. 2020, ApJL, 890, L8
van der Marel, N., Bosman, A. D., Krijt, S., Mulders, G. D., & Bergner, J. B. 2021, A&A, 653, L9
van der Plas, G., Ménard, F., Gonzalez, J. F., et al. 2019, A&A, 624, A33
Varga, J., Gerják, T., Ábrahám, P., et al. 2019, MNRAS, 485, 3112
Vioque, M., Oudmaijer, R. D., Baines, D., Mendigutía, I., & Pérez-Martínez, R. 2018, A&A, 620, A128
Vioque, M., Oudmaijer, R. D., Schreiner, M., et al. 2020, A&A, 638, A21
Wagner, K., Apai, D., Kasper, M., & Robberto, M. 2015, ApJL, 813, L2
Wang, J. J., Ruffio, J.-B., De Rosa, R. J., et al. 2015, pyKLIP: PSF Subtraction for Exoplanets and Disks, Astrophysics Source Code Library, ascl:1506.001
Wichittanakom, C., Oudmaijer, R. D., Fairlamb, J. R., et al. 2020, MNRAS, 493, 234
Zhu, Z., Hartmann, L., Calvet, N., et al. 2007, ApJ, 669, 483